Cancer cells resistant to immune checkpoint blockade acquire interferon-associated epigenetic memory to sustain T cell dysfunction

Jingya Qiu[1,2,3,12], Bihui Xu[1,2,9,12], Darwin Ye[1,2,3,4], Diqiu Ren[2,5], Shangshang Wang[1,2,3], Joseph L. Benci[1,2,10], Yuanming Xu[1,2,11], Hemant Ishwaran[6], Jean-Christophe Beltra[4,7,8], E. John Wherry [3,4,7,8], Junwei Shi [2,3,5] & Andy J. Minn [1,2,3,4,8]

Prolonged interferon (IFN) signaling in cancer cells can promote resistance to immune checkpoint blockade (ICB). How cancer cells retain effects of prolonged IFN stimulation to coordinate resistance is unclear. We show that, across human and/or mouse tumors, immune dysfunction is associated with cancer cells acquiring epigenetic features of inflammatory memory. Here, inflammatory memory domains, many of which are initiated by chronic IFN-γ, are maintained by signal transducer and activator of transcription (STAT)1 and IFN regulatory factor (IRF)3 and link histone 3 lysine 4 monomethylation (H3K4me1)-marked chromatin accessibility to increased expression of a subset of IFN-stimulated genes (ISGs). These ISGs include the RNA sensor OAS1 that amplifies type I IFN (IFN-I) and immune inhibitory genes. Abrogating cancer cell IFN-I signaling restores anti-programmed cell death protein 1 (PD1) response by increasing IFN-γ in immune cells, promoting dendritic cell and CD8+ T cell interactions, and expanding T cells toward effector-like states rather than exhausted states. Thus, cancer cells acquire inflammatory memory to augment a subset of ISGs that promote and predict IFN-driven immune dysfunction.

IFN-I and type II IFN (IFN-γ) play important roles in promoting response to ICB. These roles include enhancing expression of major histocompatibility complex class I (MHC-I) on target cells and facilitating productive interactions between T cells and dendritic cells[1–3]. However, in cancer and in chronic virus infection, persistent IFN signaling can contribute to immune suppression[4–9]. This function of IFN may relate to its role in limiting immune-mediated pathology under conditions of chronic inflammation. Besides the duration of IFN signaling, the opposing

[1]Department of Radiation Oncology, University of Pennsylvania, Philadelphia, PA, USA. [2]Abramson Family Cancer Research Institute, University of Pennsylvania, Philadelphia, PA, USA. [3]Mark Foundation Center for Immunotherapy, Immune Signaling, and Radiation, Perelman School of Medicine, University of Pennsylvania, Philadelphia, PA, USA. [4]Parker Institute for Cancer Immunotherapy, University of Pennsylvania, Philadelphia, PA, USA. [5]Department of Cancer Biology, University of Pennsylvania, Philadelphia, PA, USA. [6]Division of Biostatistics, Department of Epidemiology and Public Health, University of Miami, Miami, FL, USA. [7]Department of Systems Pharmacology and Translational Therapeutics, University of Pennsylvania, Philadelphia, PA, USA. [8]Institute of Immunology, University of Pennsylvania, Philadelphia, PA, USA. [9]Present address: Incyte, Wilmington, DE, USA. [10]Present address: Bristol Myers Squibb, Princeton, NJ, USA. [11]Present address: Pfizer, San Diego, CA, USA. [12]These authors contributed equally: Jingya Qiu, Bihui Xu. ✉e-mail: andyminn@upenn.edu

functions of this cytokine may also be determined by the type of cell that receives the signal. In human melanoma, a subset of ISGs was found to be predominantly expressed by cancer cells compared to immune cells, and expression of this set of ISGs predicts clinical resistance to ICB[7]. Accordingly, in mouse tumor models, preventing IFN-I or IFN-γ signaling in cancer cells decreases this subset of cancer-associated ISGs and can enhance the efficacy of ICB[6,7,10]. For IFN-γ, abrogating signaling in cancer cells improves the function of CD8^{+} T cells, natural killer (NK) cells, innate lymphoid cells and other innate immune populations[7]. Despite this, inhibiting IFN-γ signaling in cancer cells can come at the expense of interfering with MHC-I expression, which biases toward innate immune killing in tumors with low baseline MHC-I[7] or contributes to resistance[11,12]. Whether preventing IFN-I signaling might better enable adaptive anti-tumor immunity is unclear.

Since immune dysfunction in cancer decreases IFN levels in the tumor, the ability of cancer cells to maintain IFN-driven immunosuppression would seem difficult to sustain and even self-limiting. However, recent work suggests that acquisition of persistently increased chromatin accessibility brought about by initial activation of inflammatory signaling is one way to enhance signal strength from subsequent stimulation[13–15]. The retention of increased chromatin accessibility even after inflammatory signals abate is characteristic of inflammatory memory and is associated with H3K4me1 and transcription factors (TFs) such as AP1 and STAT3. Interestingly, ISG-high cancer cells that are resistant to ICB display epigenetic changes that partly result from chronic IFN-γ stimulation[6,16]. These epigenetic changes are characterized by altered chromatin accessibility linked to the IFN-regulated TF STAT1. However, it is unknown whether STAT1 contributes to this altered epigenome and how epigenetic changes might enhance IFN signaling in resistant tumors with attenuated levels of IFN.

Blocking the immune inhibitory receptor PD1 drives the differentiation of progenitor CD8^{+} T cells into a terminally exhausted population with limited effector and proliferative capacity compared to effector and memory T cells[17–19]. Although exhausted CD8^{+} T cells (T_{EX}) have important anti-tumor effects, inhibiting the PD1–programmed cell death ligand 1 (PDL1) axis typically does not convert T_{EX} cells into effector T cells, hence limiting the efficacy of ICB[20,21]. IFN-I signaling in T cells has been implicated in controlling the balance of these fates by acting on progenitor cells[19,22]; however, how modulating IFN-I signaling in cancer cells impacts T cell fate remains poorly defined.

Results

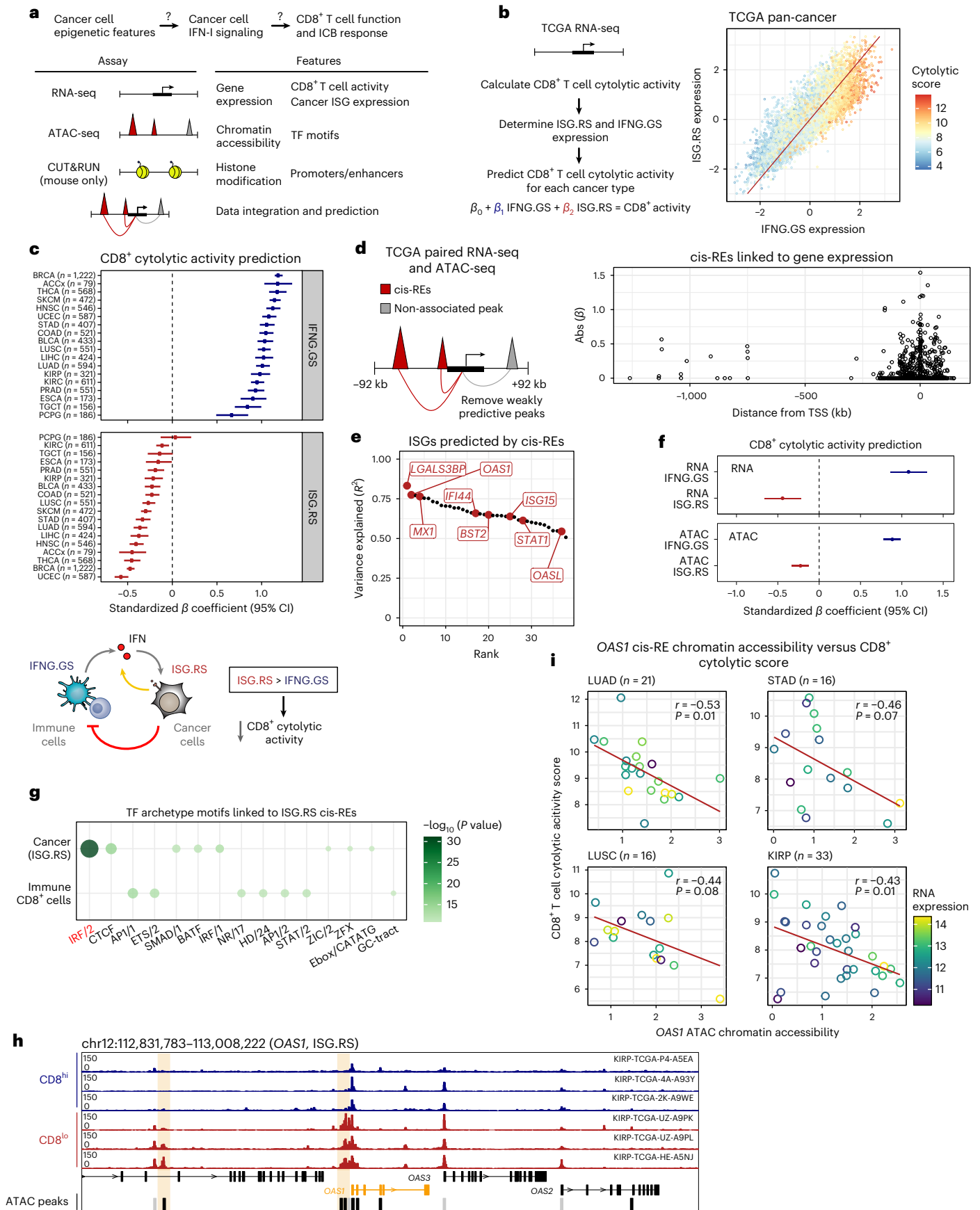### Distinct ISGs predict CD8^{+} T cell activity in human cancers

We previously identified two non-overlapping subsets of ISGs denoted ISG.RS (ISG resistance signature) and IFNG.GS (*IFNG* gene signature)[7]. The IFNG.GS sub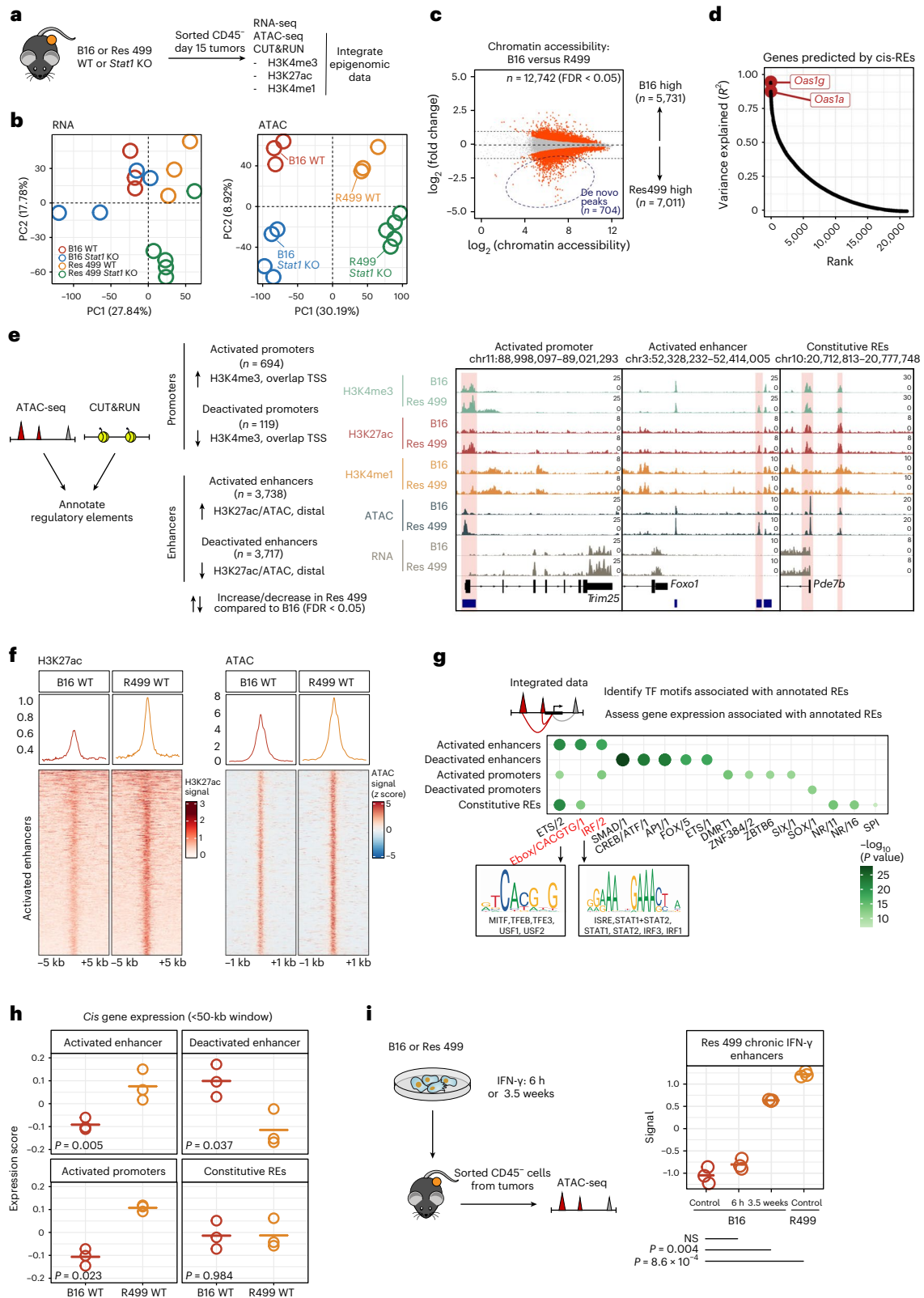set predicts clinical ICB response in patients with melanoma and is preferentially expressed by immune cells. By contrast, the ISG.RS subset consists of 38 distinct ISGs that are typically associated with IFN-I, predominantly expressed by cancer cells, and independently predicts resistance to ICB. To test whether these distinct and opposing ISGs associate with immune function broadly across human cancers, we interrogated gene expression data from a pan-cancer panel of tumors from The Cancer Genome Atlas (TCGA) ($n = 8,402$) (Fig. 1a and Extended Data Fig. 1a). For each tumor, we estimated a CD8^{+} T cell cytolytic activity score based on the expression of the CD8^{+} T cell-specific markers GZMA and PRF1 (ref. 23) (Extended Data Fig. 1b). Across all cancers, IFNG.GS expression and ISG.RS expression were positively correlated with each other, as expected (Fig. 1b). With increasing IFNG.GS expression, there was a steep increase in CD8^{+} T cell cytolytic activity but only when ISG.RS expression was relatively low (Fig. 1b, below red regression line). By contrast, when ISG.RS expression was relatively high (Fig. 1b, above red regression line), CD8^{+} T cell cytolytic activity remained blunted despite increasing IFNG.GS levels. When these data were used in a multiple regression model to estimate independent effects, across most cancer types, the IFNG.GS subset significantly predicted higher CD8^{+} T cell cytolytic activity, while the ISG.RS exhibited the opposite association (Fig. 1c). By contrast, random gene sets of similar size displayed no association with CD8^{+} T cell cytolytic activity (Extended Data Fig. 1c). Thus, distinct ISGs associated with cancer or immune cells can have opposing effects on CD8^{+} T cell activity that depend on their relative expression. These observations suggest a model in which IFNG.GS and IFN expression by immune cells can increase IFN signaling and ISG.RS expression in cancer cells, resulting in feedback inhibition and immune dysfunction characterized by high ISG.RS expression relative to IFNG.GS expression (Fig. 1c, bottom).

Because not all cancer cells appear prone to developing high ISG.RS expression relative to IFNG.GS expression, we surmised that the epigenetic state of cancer cells could be a factor. To investigate this, we integrated the subset of TCGA tumors with paired RNA sequencing (RNA-seq) and assay for transposase-accessible chromatin (ATAC) sequencing (ATAC-seq) profiles ($n = 382$) to model gene expression using chromatin accessibility features (Extended Data Fig. 1a). Briefly, for each ISG.RS gene, we constructed an elastic net linear regression model to predict RNA expression using all accessible chromatin peaks within a ±92-kb *cis*-regulatory window (median size of a mouse topologically associated domain). Because infiltrating immune cells can contribute to ATAC-seq signals in solid tumors, we filtered out known immune-specific regulatory elements[24] to focus on cancer cell-specific chromatin accessibility. This strategy allowed us to predict putative *cis*-regulatory elements (cis-REs) for ISG.RS genes and to identify ISG.RS genes with expression that is highly explained by chromatin accessibility. Each ISG.RS gene was linked to a median of six cis-REs,

Fig. 1 | Distinct ISGs and epigenetic features from cancer cells predict low CD8^{+} T cell cytolytic activity. a, Schema of genome-wide assays and deduced features to examine the relationship between cancer cell epigenetic features, IFN-I signaling and immune function. **b**, Relationship between IFNG.GS and ISG.RS expression for all TCGA tumors ($n = 8,402$), colored by CD8^{+} T cell cytolytic activity score. **c**, Standardized regression coefficients (with 95% confidence intervals (CIs)) and schema (bottom) for the effect of IFNG.GS and ISG.RS expression on CD8^{+} T cell cytolytic activity for each cancer type. Regression models for all cancer types are significant (overall *F*-test, $P < 0.001$). Bottom schema depicts a hypothetical feedback inhibition circuit between immune and cancer cells. See Genomic Data Commons (https://gdc.cancer.gov/resources-tcga-users/tcga-code-tables/tcga-study-abbreviations) for definitions for TCGA cancer type abbreviations. **d**, Distance from the TSS for all ATAC-seq peaks surrounding linked ISG.RS genes versus its standardized regression coefficient (absolute value) for predicting ISG.RS expression. Schema for integrating RNA-seq and ATAC-seq data to link peaks to genes and identify putative cis-REs is also shown. **e**, Proportion of variance explained (R^2) for ISG.RS expression from a linear model using the chromatin accessibility of putative cis-REs as independent predictors. **f**, Standardized regression

coefficients (with 95% confidence intervals) representing the effect of IFNG.GS and ISG.RS expression (top) or chromatin accessibility (bottom) on CD8^{+} T cell cytolytic activity for all cancer types with paired RNA-seq and ATAC-seq data ($n = 382$). **g**, Enrichment of archetype (non-redundant) motifs in cis-REs linked to ISG.RS genes or annotated CD8^{+} T cell-specific regulatory elements. Enrichment *P* values are shown with larger circle sizes indicating greater significance. **h**, ATAC tracks at the *OAS1* loci for representative kidney renal cell papillary cell carcinoma tumors with high (blue) or low (red) CD8^{+} T cell cytolytic activity ($n = 3$ tumors each), along with putative cis-REs (beige) that negatively correlate with CD8^{+} T cell cytolytic activity. Annotation bar (bottom) demarcates called peaks, with black and gray bars indicating putative cis-REs linked to *OAS1* and other peaks, respectively. chr, chromosome. **i**, Pearson correlation (*r*) of *OAS1* cis-RE chromatin accessibility and CD8^{+} T cell activity across all paired tumor samples for cancer types lung squamous cell carcinoma (LUSC, $n = 16$ patients), lung adenocarcinoma (LUAD, $n = 21$), stomach adenocarcinoma (STAD, $n = 16$), and kidney renal papillary cell carcinoma (KIRP, $n = 33$). Individual points are color coded by *OAS1* expression. *P* values were determined by two-sided correlation test based on Pearson's coefficient.

a Cancer cell epigenetic features → **?** → Cancer cell IFN-I signaling → **?** → CD8+ T cell function and ICB response

b TCGA RNA-seq

Calculate CD8+ T cell cytolytic activity

Determine ISG.RS and IFNG.GS expression

Predict CD8+ T cell cytolytic activity for each cancer type

$\beta_0 + \beta_1$ IFNG.GS $+ \beta_2$ ISG.RS $=$ CD8+ activity

c CD8+ cytolytic activity prediction

d TCGA paired RNA-seq and ATAC-seq

cis-REs linked to gene expression

e ISGs predicted by cis-REs

f CD8+ cytolytic activity prediction

g TF archetype motifs linked to ISG.RS cis-REs

h chr12:112,831,783–113,008,222 (*OAS1*, ISG.RS)

i *OAS1* cis-RE chromatin accessibility versus CD8+ cytolytic score

a B16 or Res 499 WT or *Stat1* KO → Sorted CD45⁻ day 15 tumors → RNA-seq, ATAC-seq, CUT&RUN - H3K4me3 - H3K27ac - H3K4me1 → Integrate epigenomic data

b RNA — PC2 (17.78%) vs PC1 (27.84%); ATAC — PC2 (8.92%) vs PC1 (30.19%). B16 WT, B16 *Stat1* KO, Res 499 WT, Res 499 *Stat1* KO

c Chromatin accessibility: B16 versus R499. n = 12,742 (FDR < 0.05). B16 high (n = 5,731); Res499 high (n = 7,011). De novo peaks (n = 704). log₂ (fold change) vs log₂ (chromatin accessibility)

d Genes predicted by cis-REs. Variance explained (R²) vs Rank. Oas1g, Oas1a

e ATAC-seq, CUT&RUN → Annotate regulatory elements. Promoters: Activated promoters (n = 694) ↑ H3K4me3, overlap TSS; Deactivated promoters (n = 119) ↓ H3K4me3, overlap TSS. Enhancers: Activated enhancers (n = 3,738) ↑ H3K27ac/ATAC, distal; Deactivated enhancers (n = 3,717) ↓ H3K27ac/ATAC, distal. ↑↓ Increase/decrease in Res 499 compared to B16 (FDR < 0.05). Activated promoter chr11:88,998,097–89,021,293 (Trim25); Activated enhancer chr3:52,328,232–52,414,005 (Foxo1); Constitutive REs chr10:20,712,813–20,777,748 (Pde7b). Tracks: H3K4me3, H3K27ac, H3K4me1, ATAC, RNA (B16/Res 499)

f H3K27ac (B16 WT, R499 WT); ATAC (B16 WT, R499 WT). Activated enhancers. H3K27ac signal (−5 kb to +5 kb); ATAC signal z score (−1 kb to +1 kb)

g Integrated data → Identify TF motifs associated with annotated REs; Assess gene expression associated with annotated REs. Activated enhancers, Deactivated enhancers, Activated promoters, Deactivated promoters, Constitutive REs. Motifs: ETS/2, Ebox/CACGTG/1, IRF/2, SMAD/1, CREB/ATF/1, AP1/1, FOX/5, ETS/1, DMRT1, ZNF384/2, ZBTB6, SIX/1, SOX/1, NR/11, NR/16, SPI. −log₁₀ (P value): 10, 15, 20, 25. MITF,TFEB,TFE3, USF1, USF2; ISRE, STAT1+STAT2, STAT1, STAT2, IRF3, IRF1

h *Cis* gene expression (<50-kb window). Expression score. Activated enhancer P = 0.005; Deactivated enhancer P = 0.037; Activated promoters P = 0.023; Constitutive REs P = 0.984. B16 WT vs R499 WT

i B16 or Res 499 → IFN-γ: 6 h or 3.5 weeks → Sorted CD45⁻ cells from tumors → ATAC-seq. Res 499 chronic IFN-γ enhancers. Signal. Control, 6 h, 3.5 weeks (B16), Control (R499). NS; P = 0.004; P = 8.6 × 10⁻⁴

consistent with previous reports of peak-to-gene links[24] (Extended Data Fig. 1d). Strongly linked ISG.RS cis-REs were enriched at promoter-proximal regions, as well as in distal regions over 100 kb upstream and downstream of transcription start sites (TSSs; Fig. 1d). Expression of most ISG.RS genes is highly explained by chromatin accessibility, indicative of epigenetic regulation (Fig. 1e).

Similar to RNA expression, chromatin accessibility of ISG.RS cis-REs was also negatively associated with CD8⁺ T cell cytolytic activity,

in contrast to cis-REs linked to IFNG.GS genes (Fig. 1f). A search for TF motifs enriched in these cis-REs uncovered the IRF/2 archetype (non-redundant) motif. This motif is associated with TFs regulated by IFN and pattern-recognition receptor (PRR) signaling, including STAT1 and members of the IRF family (Fig. 1g). Notably, the IRF/2 motif is not enriched in immune-specific regulatory elements, suggesting that factors involved in ISG.RS and IFNG.GS regulation are distinct. One ISG.RS gene with evidence of strong epigenetic regulation is *OAS1* (Fig. 1e).

Fig. 2 | Widespread remodeling of the relapsed tumor epigenome is characterized by activated enhancers with ISRE-like motifs. a, Schematic for multiomic profiling of B16 and Res 499 tumors, with or without *Stat1* KO. **b**, Principal-component analysis (PCA) of RNA expression (left) and chromatin accessibility (right) for B16 and Res 499 (R499) cancer cells with or without *Stat1* KO, sorted from in vivo tumors (B16 and Res 499, $n = 3$; B16 *Stat1* KO, $n = 4$; Res 499 *Stat1* KO, $n = 5$ mice). PC, principal component. **c**, Mean chromatin accessibility and $\log_2$ fold change between B16 and Res 499 cells for all consensus ATAC peaks. Red dots indicate peaks that are significantly differentially accessible between B16 and Res 499 cells (false discovery rate (FDR) < 0.05). **d**, Variance explained (R^2) for gene expression from a linear model using the chromatin accessibility of putative cis-REs. **e**, Schema and criteria for annotating regulatory elements (REs; left) and representative tracks (right) for activated promoters, activated enhancers, or constitutive regulatory elements in Res 499 cells compared to B16 cells. **f**, Heatmap of H3K27ac and ATAC signal intensity over Res 499 activated enhancers ($n = 2$ mice per condition for the

H3K27ac assay, $n = 5$ mice per condition for the ATAC assay). **g**, Enrichment of archetype motifs in annotated regulatory elements that are activated, deactivated, or constitutive between Res 499 and B16 cells. Enrichment P values are shown with larger circle sizes indicating greater significance. Boxes for highlighted archetype motifs contain the motif logo and select TF motifs belonging to the archetype motif group. Schema for use of the integrated multiomic data for **g**,**h** is shown above. **h**, Gene set enrichment score of genes located within a 50-kb *cis*-regulatory window of the specified set of annotated regulatory elements in B16 or Res 499 cancer cells ($n = 3$ mice per condition). P values were determined by two-sided t-test. **i**, Summary ATAC enrichment score for a subset of Res 499 activated enhancers (900 of 3,738) induced by chronic IFN-γ in cancer cells sorted from the indicated in vivo tumors ($n = 3$ mice per condition). B16 tumors were treated with IFN-γ in vitro for 6 h (acute) or 3.5 weeks (chronic) before implantation into mice (schema, left). P values were calculated from two-sided t-tests. NS, not significant.

In several cancer types, proximal and distal cis-REs linked to *OAS1* are inaccessible in tumors with high CD8⁺ T cell cytolytic activity but are strikingly accessible in tumors with low CD8⁺ T cell activity (Fig. 1h,i and Extended Data Fig. 2a–c). Together, these data reveal a relationship between cancer cell epigenetic features, high cancer cell-intrinsic ISG.RS expression, and immune dysfunction. ISG.RS genes such as *OAS1* link these relationships in multiple human cancers.

Widespread epigenetic remodeling of ICB-resistant tumors

Because epigenetic features associated with elevated ISG.RS in human cancer cells can predict low CD8⁺ T cell cytolytic activity, we next investigated how the chromatin landscape of cancer cells can promote high ISG.RS expression and how this contributes to immunotherapy resistance. Toward this end, we employed the mouse tumor model Res 499, which was derived from an ICB-relapsed B16-F10 (B16) melanoma tumor and exhibits high expression of ISG.RS[16]. Examination of ATAC-seq data from B16 and Res 499 cancer cells sorted from mouse tumors revealed that ICB-resistant Res 499 cancer cells have highly distinct epigenomes compared to B16 cells (Fig. 2a,b and Extended Data Fig. 3a). About 15% of the 87,697 consensus peaks were significantly altered in Res 499, indicating dramatic remodeling of the chromatin landscape (Fig. 2c). Genome-wide modeling of gene expression using chromatin accessibility (Extended Data Fig. 1a) revealed that *Oas1g* and its paralog *Oas1a* were among the top genes predicted to be regulated by putative cis-REs (Fig. 2d). These *Oas1* genes are orthologs to human *OAS1*, which also exhibits expression that is strongly associated with epigenetic changes in human TCGA tumors (Fig. 1e). Thus, these data suggest that, similar to human tumors, mouse tumors also reveal a relationship between cancer cell epigenetic features, expression of ISGs such as *Oas1*, and immune dysfunction.

To map the cancer cell epigenetic changes associated with ICB resistance to regulatory elements, we used the same collection of B16 and Res 499 tumors to perform genome-wide in vivo cleavage

under targets and release using nuclease (CUT&RUN) analysis for the active promoter mark histone 3 lysine 4 trimethylation (H3K4me3), the active enhancer mark histone 3 lysine 27 acetylation (H3K27ac), and the enhancer mark H3K4me1 (Fig. 2a and Extended Data Fig. 3b). We integrated these epigenomic data to annotate an in vivo catalog of promoters and enhancers (Extended Data Fig. 3c) that are either activated, deactivated, or constitutive in Res 499 tumors relative to B16 tumors (Fig. 2e and Extended Data Fig. 3d). Most regulatory elements with significantly altered activity are enhancers in distal intergenic or intronic regions (Extended Data Fig. 3e) exhibiting greater H3K27ac signal and ATAC chromatin accessibility (Fig. 2f). Of the 3,738 enhancers with increased H3K27ac activity in Res 499 cells, which we denote as Res 499 activated enhancers, the majority have pre-existing chromatin accessibility in B16 cells, while only about 10% are acquired de novo (Extended Data Fig. 3f). Analysis of associated TF motifs revealed that enhancers and promoters activated in Res 499 cells are enriched for the IRF/2 archetype motif that represents IFN-stimulated response elements (ISRE) predicted to accommodate STAT1–STAT2 heterodimers and IRF family TFs (Fig. 2g). This IRF/2 motif is the same motif enriched in putative cis-REs linked to cancer cell ISG.RS genes in TCGA tumors (Fig. 1g). Consistent with this, paired RNA-seq data revealed that genes within a 50-kb *cis*-regulatory window flanking the activated enhancers exhibit elevated expression in Res 499 tumors (Fig. 2h) and are enriched for genes belonging to the Janus kinase (JAK)–STAT signaling pathway (Extended Data Fig. 3g). Thus, similar to human tumors, widespread in vivo chromatin remodeling in ICB-resistant Res 499 cancer cells is characterized by activated ISRE-related enhancers linked to genes associated with IFN signaling.

ICB-resistant tumors acquire inflammatory memory domains

Previously, we showed that chronic IFN-γ stimulation of B16 cells for 3 weeks in vitro is sufficient to increase STAT1 levels, instigate epigenetic changes that partially overlap with those of ICB-relapsed Res 499

Fig. 3 | Tumors resistant to ICB are characterized by H3K4me1-marked inflammatory memory domains regulated by STAT1 and IRF3. a, Schema for identifying IFN-associated inflammatory memory domains (IFN-IMDs) in the context of acquired resistance. IFN signaling is terminated in vivo by *Stat1* KO to reveal either persistent H3K4me1 and chromatin accessibility (memory domains) or non-persistent chromatin features (resolved domains). **b**,**c**, Summary enrichment scores (**b**) and representative tracks (**c**) for H3K27ac, H3K4me1, or ATAC signal at IFN-IMDs or resolved domains in cancer cells sorted from the indicated in vivo tumors ($n = 2$ mice per condition for each assay). Red bars overlaid on tracks highlight IFN-IMDs or resolved domains. P values were determined by one-way ANOVA with post hoc Tukey's honest significant difference (HSD) test. DKO, double KO; SKO, *Stat1* KO. **d**, Genomic regions where IFN-IMDs reside (top) and percent of IFN-IMDs that overlap Res 499 activated enhancers (bottom). UTR, untranslated region. **e**, TF motifs enriched in inflammatory memory domains. P values are color coded, and larger circle sizes

indicate greater significance. Motifs highlighted in red are associated with IFN signaling, and motifs in blue are associated with inflammatory memory. **f**, Summary enrichment scores for the inflammatory memory gene signature (left) and top gene ontology biological process terms enriched in this gene set (right) ($n = 3, 5, 3$ and 5 mice per condition, from left to right). P values were determined by two-sided t-test. **g**, $\log_2$ fold changes in expression of individual ISG.RS genes between Res 499 and B16 in vivo tumors. IFN-associated inflammatory memory genes are denoted in orange; non-memory genes are denoted in gray. **h**, Expression of ISG.RS genes (RNA) or H3K27ac, H3K4me1, or ATAC signal intensity at cis-REs linked to these genes in cancer cells sorted from the indicated in vivo tumors ($n = 3, 5, 3$ and 5 mice per condition for the RNA assay; $n = 2$ mice per condition for H3K27ac and H3K4me1 assays; $n = 5$ mice per condition for the ATAC assay). P values were determined by one-way ANOVA with post hoc Tukey's HSD test. Box plots represent the 25th percentile, the median, the 75th percentile and 1.5× interquartile range (IQR) (whiskers).

tumors, and confer ICB resistance[6]. Therefore, to examine whether the Res 499 activated enhancers are also linked to chronic IFN-γ signaling, we stimulated B16 cells for either 6 h (acute) or 3.5 weeks (chronic) in vitro before implantation into syngeneic mice and profiled the

resulting established tumors by ATAC-seq. We observed that chronic IFN-γ stimulation, but not acute stimulation, led to increased chromatin accessibility in vivo at about one-quarter of Res 499 activated enhancers (Fig. 2i and Extended Data Fig. 3h). These chronic IFN-γ-induced
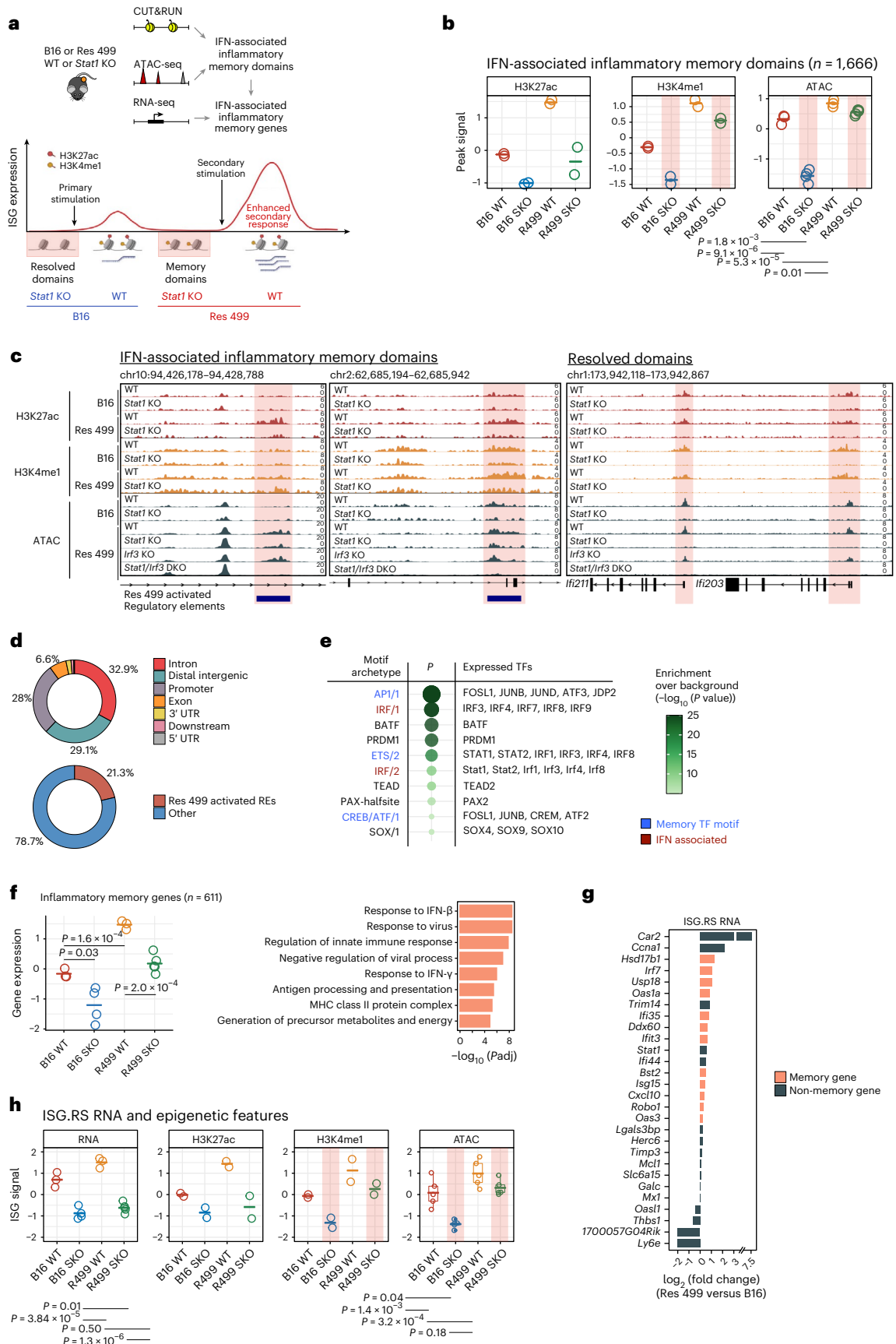
enhancers were also specifically enriched with IRF/2 motifs (Extended Data Fig. 3i). Conversely, to determine whether preventing IFN-γ signaling could impact epigenetic changes in Res 499 tumors in vivo, we deleted *Stat1* in Res 499 cancer cells before implantation into mice. Surprisingly, although STAT1 footprints were associated with IRF/2 motifs (Extended Data Fig. 3j) and H3K27ac levels decreased at Res 499 activated enhancers upon *Stat1* knockout (KO), levels of chromatin accessibility and H3K4me1 levels persisted (Extended Data Fig. 4a). This persistence of chromatin accessibility and H3K4me1 at Res 499 activated enhancers in the absence of active IFN signaling is reminiscent of epigenetic features of inflammatory memory. Thus, ICB-resistant cancer cells may retain memory of chronic IFN signaling in chromatin domains.

Chromatin regions that gain accessibility during an inflammatory response but remain accessible after signal termination in order to enhance future responses have been defined as inflammatory memory domains[15,25]. To formally define inflammatory memory domains in the context of chronic IFN-driven ICB resistance, we identified all chromatin domains that uniquely maintain persistent chromatin accessibility in Res 499 tumors compared to B16 tumors after preventing IFN signaling by *Stat1* KO (Fig. 3a and Methods). Upon STAT1 loss, these IFN-associated inflammatory memory domains (IFN-IMDs) lost the active enhancer mark H3K27ac in both B16 and Res 499 cells but retained chromatin accessibility and H3K4me1 deposition in Res 499 tumors only (Fig. 3b,c). By contrast, although 'resolved domains' were also associated with IFN-related pathways (Extended Data Fig. 4b), they did not maintain persistent chromatin accessibility and H3K4me1 with STAT1 loss (Fig. 3c and Extended Data Fig. 4c). Approximately 21% of IFN-IMDs overlapped with Res 499 activated enhancers (Fig. 3d), which covered enhancers that are related to cytokines and processes other than IFN (Extended Data Fig. 3g). IFN-IMDs are enriched with not only the archetype motif IRF/2, comprising IFN signaling TFs (for example, STAT1, IRF3 and IRF1), but are also co-enriched for known inflammatory memory TFs belonging to the AP1, ETS and ATF families[25] (Fig. 3e).

Next, to define putative inflammatory memory genes, we used a correlation-based method to identify gene expression linked to IFN-IMD chromatin accessibility after chronic (3.5 weeks) but not acute IFN-γ stimulation. This resulted in increased expression of 611 IFN-IMD-linked inflammatory memory genes in vivo (Extended Data Fig. 4e). These genes were also elevated in Res 499 tumors, consistent with Res 499 activated enhancers arising at least partly from chronic IFN-γ signaling. Inflammatory memory genes include IFN-I response and viral defense genes (Fig. 3f), the majority of which also had elevated expression in resistant tumors compared to sensitive tumors in vivo (Extended Data Fig. 4f). Importantly, most ISG.RS genes are included in these inflammatory memory genes (Fig. 3g). Indeed, direct examination of cis-REs associated with ISG.RS genes confirms that, when IFN signaling is prevented with *Stat1* KO, H3K27ac activity and RNA expression decreases but H3K4me1 and chromatin accessibility remain elevated in Res 499 cells compared to B16 cells (Fig. 3h).

In sum, these findings suggest that Res 499 tumors are characterized by H3K4me1-marked IFN-IMDs and increased expression of a subset of linked ISGs that prominently includes ISG.RS genes. Thus, elevated ISG.RS expression represents the acquisition of ICB resistance and epigenetic features of IFN-associated inflammatory memory.

The OAS1 pathway amplifies cancer cell IFN-I signaling

Because inflammatory memory domains are thought to support enhanced transcriptional responses to subsequent inflammatory stimulation[26], we considered that ICB-resistant cancer cells using IFN-I signaling to promote immune dysfunction may benefit from these attributes. Specifically, as cancer cells use IFN-I to drive ICB resistance, ensuing immune dysfunction would be expected to decrease IFN-I levels in the tumor and impede cancer cells from sustaining IFN-driven resistance. Indeed, single-cell RNA sequencing (scRNA-seq) of immune populations from anti-PD1-treated or untreated Res 499 tumors revealed that *Ifnb1* levels are low but increase with deletion of the IFN-I receptor (IFNAR) in cancer cells (Extended Data Fig. 5a), suggesting that IFN-I signaling in resistant cancer cells can attenuate IFN-I levels in the tumor. Thus, we sought to determine whether IFN-IMDs may enable cancer cells to amplify IFN-I signaling, sustain high ISG.RS expression, and maintain immune dysfunction as suggested by our TCGA analysis (Fig. 1c, yellow arrow in bottom schema).

Notably, the ISG.RS gene *Oas1*, which is one of the top ISGs that link epigenetic features to ICB resistance (Figs. 1e and 2d), is a cytosolic RNA PRR evolutionarily related to the DNA sensor cGAS and implicated in amplifying the IFN-I response through the downstream RNA sensor RIG-I[27,28] (Fig. 4a). Res 499 cells exhibited markedly higher tonic (baseline) levels of *Oas1* transcript and OAS1 protein in vitro compared to B16 cells (Fig. 4b and Extended Data Fig. 5b). Similar findings were observed with Res 237 mouse breast cancer cells derived from an ICB-relapsed TSA tumor (Extended Data Fig. 5c,d). Therefore, to determine whether elevated OAS1 levels enable ICB-resistant cancer cells to amplify IFN-I signaling and maintain high ISG.RS expression, we deleted *Oas1* by CRISPR. At baseline, despite IFN-I levels being too low for detection by protein, KO of *Oas1a* and *Oas1g* diminished the higher tonic ISG expression found in ICB-resistant Res 499 and Res 237 cells compared to that in their ICB-sensitive parental counterparts (Fig. 4c). After stimulation with the double-stranded RNA mimetic polyI:C, Res 499 and Res 237 cells also generated greater amounts of IFN-I and induced higher levels of ISGs than parental cells, a property that was also largely abrogated by *Oas1* KO (Fig. 4d and Extended Data Fig. 5e–g). In sum, these results suggest that ICB-resistant cancer cells can amplify IFN-I signaling through the OAS1 pathway, possibly enabled by IFN-IMDs.

### IRF3 and STAT1 establish inflammatory memory domains

We next sought to understand how the ability of OAS1 to amplify IFN-I signaling may result from and/or promote IFN-IMDs. Besides STAT1, the IRF/2 archetype motif that is enriched in Res 499 activated enhancers

---

Fig. 4 | OAS1 is controlled by inflammatory memory domains and amplifies IFN-I signaling in ICB-resistant cancer cells. a, Model for OAS1 regulation of IFN-I signaling. dsRNA, double-stranded RNA. **b**, Protein expression of OAS1 in B16 and Res 499 cells in vitro. The image shown is representative of two technical repeats. **c**, Gene set enrichment analysis (GSEA) of IFN-I-related ISGs in Res 499 wild-type (WT) versus Res 499 *Oas1*-KO cells (left) and Res 237 WT versus Res 237 *Oas1*-KO cells (right), both in vitro. NES, normalized enrichment score. **d**, Concentration of IFN-α protein (left; B16, n = 6; Res 499, n = 12; Res 499 *Oas1* KO, n = 8) and relative RNA expression of indicated ISGs (middle and right; B16, n = 4; Res 499, n = 11; Res 499 *Oas1* KO, n = 7) following polyI:C transfection of B16, Res 499 or Res 499 *Oas1*-KO cells in vitro (n represents biological replicates). **e**, H3K27ac, H3K4me1, ATAC, and RNA signal tracks of the *Oas1a–Oas1g* locus from B16 or Res 499 (R499), B16 or Res 499 *Stat1*-KO (SKO), Res 499 *Irf3*-KO (IKO), and Res 499 *Stat1*- and *Irf3*-double KO (DKO) cells sorted from in vivo tumors. Highlighted regions (red) indicate putative IFN-IMDs linked to *Oas1a–Oas1g*. Average signal of the highlighted regions is summarized in the

right-hand margin (n = 2 mice per condition for H3K27ac and H3K4me1 assays; n = 3, 2, 4, 3, 4 and 3 mice per condition for the ATAC assay). **f**, Summary ATAC enrichment scores at putative cis-REs of ISG.RS genes in cancer cells sorted from the indicated in vivo tumors (B16, n = 3; B16 SKO, n = 2; Res 499 WT, n = 4; Res 499 SKO, n = 3; Res 499 *Irf3* KO, n = 4; Res 499 DKO, n = 3 mice). **g**, Summary ATAC enrichment scores at IFN-IMDs (left), heatmap of chromatin accessibility at individual IFN-IMDs (middle), and summary ATAC enrichment scores at resolved domains (right) in cancer cells sorted from the indicated in vivo tumors (n = 3, 2, 4, 3, 4 and 3 mice per condition). **h**, Survival of mice with Res 499 WT or *Oas1*-KO tumors either untreated (NT) or treated with anti-CTLA4 plus anti-PDL1 (NT, n = 10; anti-CTLA4 and anti-PDL1, n = 27 mice for each genotype). **i**, Survival of mice with B16 or Res 499 WT or *Ddx58* (gene for RIG-I) KO tumors treated with or without anti-CTLA4 plus anti-PD1 antibodies (untreated, n = 5; ICB, n = 10 mice for each genotype). P values were determined by two-sided t-test or log-rank test for survival. Box plots represent the 25th percentile, the median, the 75th percentile and 1.5× IQR (whiskers).

---

and IFN-IMDs (Figs. 2g and 3e) also accommodates several IRF family members. Moreover, IRFs are expected to be activated by the OAS1 pathway, similar to STAT1 activation by IFN-I signaling, suggesting a possible feedforward mechanism (Fig. 4a). To determine whether STAT1 and IRFs control increased tonic OAS1 levels, we first performed small interfering (si)RNA knockdown for various IRFs in either control

or *Stat1*-KO Res 499 cells. This revealed that knockdown of *Irf3*, but not other IRF genes tested, cooperated with *Stat1* KO to diminish *Oas1* levels (Extended Data Fig. 5h). Examination of a 50-kb *cis*-regulatory window for *Oas1* uncovered two H3K27ac-marked IFN-IMDs (which are also Res 499 activated enhancers) that were highly predictive of *Oas1* expression (Fig. 4e). Accordingly, when IFN signaling was prevented with
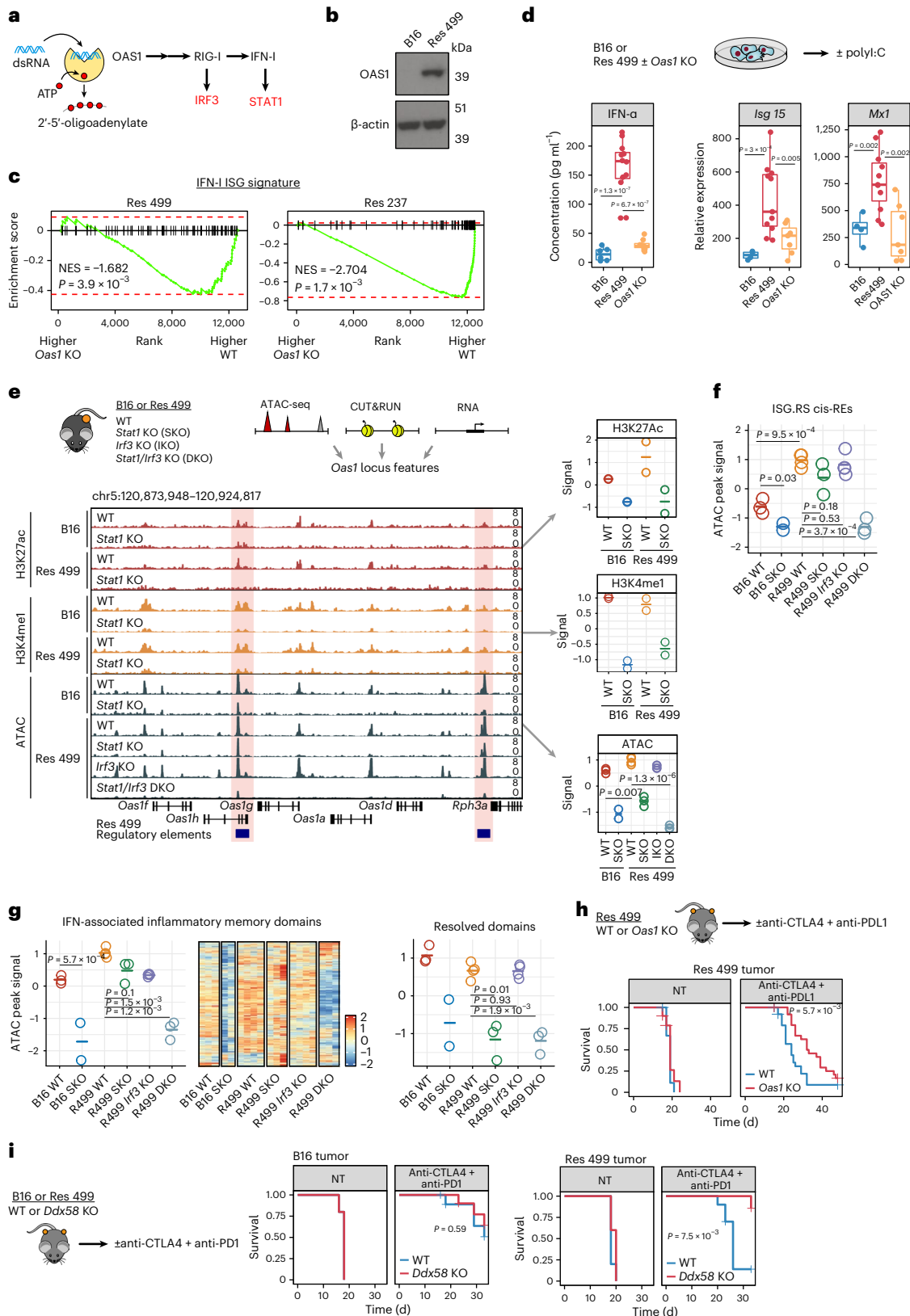
Stat1 KO, H3K27ac activity in these domains decreased, but H3K4me1 and chromatin accessibility remained elevated in Res 499 tumors compared to B16 tumors. CRISPR-mediated co-deletion of *Irf3* along with *Stat1* abrogated this persistent chromatin accessibility (Fig. 4e, right). In fact, co-deletion of *Stat1* and *Irf3*, but not deletion of either alone, largely abrogated chromatin accessibility of cis-REs from ISG.RS genes (Fig. 4f) and of the majority of IFN-IMDs and Res 499 activated enhancers genome-wide (Fig. 4g and Extended Data Fig. 5i). By contrast, *Irf3* deletion was inconsequential for the chromatin accessibility of resolved domains, which were STAT1 dependent (Fig. 4g, right). In total, these results suggest that Res 499 activated enhancers and IFN-IMDs are initiated by STAT1, leading to high levels of ISG.RS genes such as *Oas1*. OAS1 then amplifies IFN-I and PRR signaling when IFN in the tumor is attenuated, enabling STAT1 and IRF3 to maintain IFN-IMDs and enhanced ISG expression through a feedforward loop.

OAS1 and the IFN-I pathway in cancer cells inhibit ICB response

Having linked epigenetic changes in ICB-resistant tumors with features of inflammatory memory and the ability to amplify IFN-I signaling, we next sought to understand how these properties help to sustain ICB resistance. KO of *Oas1a* and *Oas1g* in either ICB-resistant Res 499 or Res 237 cells restored the response to anti-cytotoxic T lymphocyte-associated protein 4 (CTLA4) plus anti-PDL1 or anti-CTLA4 therapy alone, respectively (Fig. 4h and Extended Data Fig. 6a), and was accompanied by greater abundance of intratumoral CD8$^+$ T cells (Extended Data Fig. 6b). Consistent with OAS1 regulating ICB resistance through RIG-I and IFN-I signaling, KO of *Ddx58* (gene for RIG-I) (Fig. 4i) or *Ifnar1* (Fig. 5a and Extended Data Fig. 6c), or delayed administration of a JAK inhibitor (Extended Data Fig. 6d) also re-sensitized Res 499 tumors to anti-PD1 and/or anti-PDL1 ± anti-CTLA4 therapy and improved infiltration of total CD8$^+$ T cells (Fig. 5b) and PRF1$^+$CD8$^+$ T cells (Extended Data Fig. 6e). Notably, improved response from deletion of either *Ddx58* or *Ifnar1* was specifically observed for Res 499 tumors but not B16 tumors (Fig. 4i and Extended Data Fig. 6f). Although disrupting IFN-I signaling can improve ICB response for treatment-naive tumors, as in the case of CT26 colorectal tumors (Extended Data Fig. 6g), this preference for Res 499 versus B16 tumors highlights how cancer cell IFN-I signaling can specifically drive acquired ICB resistance. Thus, blocking cancer cell IFN-I signaling or the upstream RNA PRRs that amplify this pathway can improve ICB efficacy, particularly in the context of acquired resistance and IFN-related inflammatory memory.

To further understand how inhibiting cancer cell IFN-I signaling restores response in the context of acquired ICB resistance, we opted to focus on the direct effects of *Ifnar1* KO on anti-PD1 efficacy in the Res 499 model. Here, improved anti-PD1 response from *Ifnar1* KO was accompanied by greater MHC-I levels on cancer cells (Fig. 5c), required cancer cell MHC-I expression (Fig. 5a), and was highly dependent on CD8$^+$ T cells and host PRF1, while being comparatively less dependent on NK1.1$^+$ innate immune cells (Fig. 5a and Extended Data Fig. 6h,i). Intriguingly, the improvement in CD8$^+$ T cell infiltration and anti-PD1

response after *Ifnar1* KO was evident even when a minority of cancer cells were unable to signal through IFNAR (Fig. 5d,e), suggesting that blocking cancer cell IFN-I signaling principally restores a missing function important for T cell activation rather than mitigates an inhibitory function that prevents immune-mediated killing. Indeed, *Ifnar1* KO in Res 499 cells decreased expression of many genes previously demonstrated to promote anti-PD1 resistance[29] including genes that may alter inflammatory cytokine production (for example, *Otulin*, *Rnf31*, *Adar*) (Fig. 5f). By contrast, preventing IFN-γ receptor signaling by KO of *Ifngr1* in Res 499 cancer cells did not increase MHC-I (Fig. 5c), required a majority of cells to have *Ifngr1* KO to restore ICB response (Fig. 5d), and most strongly decreased expression of genes that either control MHC-I antigen presentation or retard innate immune recognition (for example, *Tap1*, *Tap2*, *H2-T23*) (Fig. 5f), which is consistent with *Ifngr1* KO facilitating innate immune killing of Res 499 tumors[7]. In total, these findings suggest that interfering with cancer cell IFN-I signaling restores the anti-tumor response primarily at an early step important for T cell activation and differentiation rather than at a later step that alters the cell-intrinsic sensitivity to immune-mediated killing.

The cancer cell IFN-I pathway controls immune cell interactions

Because a minority of cancer cells with *Ifnar1* KO is sufficient to improve a CD8$^+$ T cell-driven ICB response, this suggests that IFN-I signaling in cancer cells results in a loss of function important for T cell activation or differentiation. To investigate this notion, we examined the immune populations of Res 499 tumors using scRNA-seq. Surprisingly, this revealed that KO of *Ifnar1* in cancer cells was sufficient to increase immune cell expression of IFNG.GS, particularly in dendritic cells (DCs) and myeloid cells (Fig. 6a,b and Extended Data Fig. 7a). This was accompanied by an increase in *Ifng* expression in NK cells and in CD8$^+$ T cells (Fig. 6c). An increase in IFN-γ expression by CD8$^+$ T cells was confirmed by flow cytometry and was particularly evident in effector-like and exhausted subsets (Extended Data Fig. 7b). Importantly, these increases in IFNG.GS and *Ifng* expression were observed even in the absence of anti-PD1 therapy, suggesting that blocking cancer cell IFN-I signaling alone initiates favorable changes in the immune microenvironment that are further enhanced by addition of anti-PD1 therapy. Thus, these findings suggest that inhibiting IFN-I signaling in cancer cells increases IFNG.GS and IFN-γ expression in immune cells.

DCs can generate critical cytokines to enhance CD8$^+$ T cell recruitment and activation[30,31]. The production of IFN-γ by T cells can then further facilitate interactions with DCs that are important for anti-PD1 response. To determine whether the higher IFNG.GS expression observed in DCs and the enhanced *Ifng* production by CD8$^+$ T cells are associated with changes consistent with enhanced interaction between CD8$^+$ T cells and DCs, we used scRNA-seq data to first identify four major DC subtypes in Res 499 tumors, namely, DC1, DC2, DC3 and plasmacytoid DC (pDC), using gene sets for each DC subtype[32] (Fig. 6d,e and Extended Data Fig. 7c). Next, we inferred cell–cell interaction

---

Fig. 5 | Blocking OAS1 and IFN-I signaling in tumor cells restores CD8$^+$ T cell-driven response to ICB. a, Survival of mice with Res 499 WT, Res 499 *Ifnar1*-KO or Res 499 *Ifnar1*- and *B2m*-double-KO tumors, either untreated or treated with anti-PD1 therapy. NK or CD8$^+$ T cells were depleted with anti-NK1.1 or anti-CD8 antibodies, respectively, or perforin$^{-/-}$ mice (*Prf1$^{-/-}$*) were used to prevent perforin-mediated killing. Untreated WT, *n* = 5 mice; anti-PD1, WT, *n* = 4 mice; untreated *Ifnar1*-KO, *n* = 24 mice; anti-PD1, *Ifnar1*-KO, *n* = 24 mice; untreated *Ifnar1*- and *B2m*-KO, *n* = 5 mice; anti-PD1, *Ifnar1*- and *B2m*-KO, *n* = 5 mice; untreated *Ifnar1*-KO, anti-NK1.1, *n* = 10 mice; anti-PD1, *Ifnar1*-KO, anti-NK1.1, *n* = 15 mice; untreated *Ifnar1*-KO, anti-CD8, *n* = 10 mice; anti-PD1, *Ifnar1*-KO, anti-CD8, *n* = 10 mice; untreated *Ifnar1*-KO *Prf1$^{-/-}$*, *n* = 2 mice; anti-PD1, *Ifnar1*-KO *Prf1$^{-/-}$*, *n* = 4 mice. **b**, Percent of tumor-infiltrating CD8$^+$ T cells in total CD45$^+$ cells from mice with Res 499 WT or Res 499 *Ifnar1*-KO tumors, untreated or treated with anti-PD1 therapy (untreated WT, *n* = 22 mice; untreated KO, *n* = 25 mice;

anti-PD1, WT, *n* = 32 mice; anti-PD1, KO, *n* = 29 mice). **c**, Median fluorescence intensity (MFI) values of surface MHC-I expression on cancer cells from Res 499 WT, Res 499 *Ifnar1*-KO, or Res 499 *Ifngr1*-KO tumors assessed with an anti-MHC-I antibody or an isotype IgG control (*n* = 5 biological replicates per group). **d,e**, Day 15 tumor volume (**d**) and percent tumor-infiltrating CD8$^+$ T cells (**e**) after anti-PD1 treatment of mice injected with a mixture of Res 499 WT and *Ifnar1*-KO cells or *Ifngr1*-KO cells. The percentage of control to KO cells is depicted (*n* = 5 mice per group). **f**, GSEA of genes conferring resistance to anti-PD1-based therapy[29] comparing cancer cells sorted from Res 499 WT tumors versus cells sorted from either *Ifnar1*-KO tumors (left) or *Ifngr1*-KO tumors (right). Shown are normalized enrichment scores and *P* values. Heatmap depicts relative gene expression of the leading-edge genes. *P* values were determined by two-sided *t*-test or log-rank test for survival. Box plots represent the 25th percentile, the median, the 75th percentile and 1.5× IQR (whiskers).

strength between the DC subsets and CD8$^+$ T cells using CellChat[33]. For Res 499 tumors lacking IFNAR and treated with anti-PD1 therapy, the strongest predicted interaction was between CD8$^+$ T cells and the DC3 subtype (Fig. 6f). This was driven by an increased communication probability between multiple co-stimulatory ligands on DCs with their receptors on CD8$^+$ T cells, including CD86 with CD28, interleukin (IL)-15 with IL-5RA and IL-2RB, and 4-1BB ligand (TNFSF9) with 4-1BB (TNFRSF9) (Fig. 6g). The collective expression of these receptor–ligand

pairs was augmented by tumor *Ifnar1* KO and was further enhanced by anti-PD1 therapy (Fig. 6h and Extended Data Fig. 7d). Similar results were uncovered using scTensor[34] (Extended Data Fig. 7e). Flow cytometry confirmed that KO of *Ifnar1* in Res 499 cancer cells resulted in higher expression of ligands such as CD86 on CD11c$^+$ DCs (Extended Data Fig. 7f), and KO of host *Batf3*, which was expressed by the DC3 subset (Extended Data Fig. 7c), abrogated the ability of tumor *Ifnar1* KO to restore response to anti-PD1 therapy (Extended Data Fig. 7g).
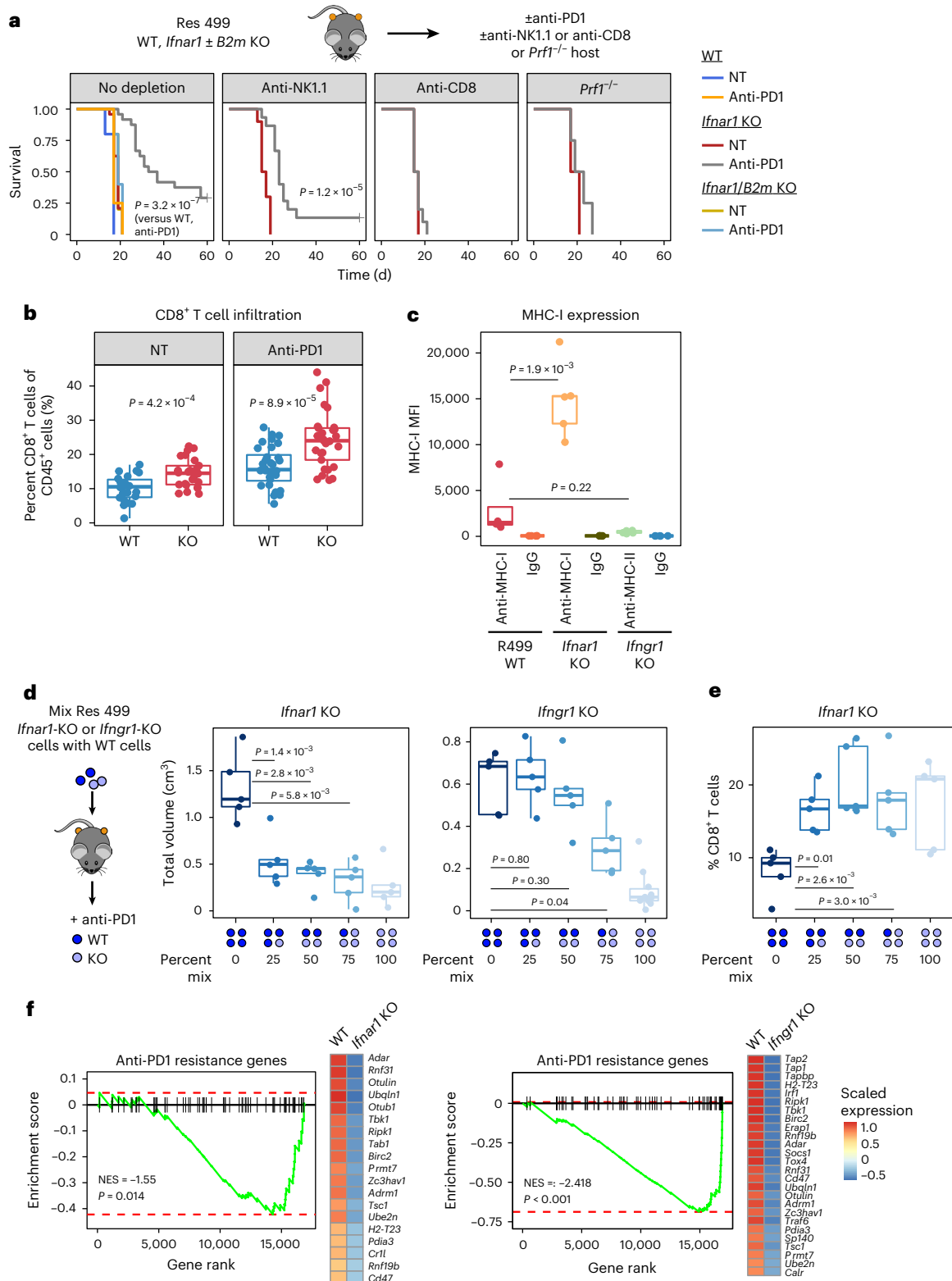
Thus, these data suggest that blocking IFN-I signaling in cancer cells promotes critical receptor–ligand interactions between CD8+ T cells and DC3 cells, contributing to restored immune cell IFN-γ signaling.

The cancer cell IFN-I pathway impacts CD8+ T cell state transition

Enhanced interactions between CD8+ T cells and DC3 cells that occur after cancer cell *Ifnar1* KO might impact the fate of CD8+ T cells. To investigate this, we directed our focus to CD8+ T cells sorted from Res 499 tumors. By scRNA-seq and trajectory analysis, six major T cell states were identified (Fig. 7a). Here, each T cell state was first classified as exhausted or non-exhausted using a core signature for PD1+ T_{EX} cells. Next, the non-exhausted states were further classified into naive-like ($T_{naive-like}$) and effector-like ($T_{EFF-like}$) T cell subsets, while the exhausted states were further divided into progenitor T_{EX} (T_{EX}^{prog1} and T_{EX}^{prog2}), intermediate T_{EX} (T_{EX}^{int}) and terminal T_{EX} (T_{EX}^{term}) populations (Fig. 7a and Extended Data Fig. 8a). Analysis of select marker genes (*Tox, Tcf7, Tbx21, Klrg1, Cx3cr1, Cxcr5, Gzmb, Mki67)* supported these classifications (Extended Data Fig. 8b). For Res 499 tumors, the majority of intratumoral CD8+ T cells resided in the T_{EX}^{prog2} state (Fig. 7b). Upon anti-PD1 treatment, there was an increase in T_{EX}^{int} and T_{EX}^{term} cells at the expense of cells occupying the non-exhausted $T_{EFF-like}$ state, consistent with anti-PD1 therapy pushing T_{EX}^{prog2} cells further toward T_{EX}^{int} and then T_{EX}^{term} states. However, although the proportion of T_{EX}^{term} cells still increased after treating mice with *Ifnar1*-KO Res 499 tumors with anti-PD1 therapy, there was a notable expansion of $T_{EFF-like}$ cells when cancer cells could not signal through IFNAR (Fig. 7b and Extended Data Fig. 8c). This was confirmed with flow cytometry by examining CD8+ T cells that were PD1lo/hiTIM3−CX3CR1+ (Extended Data Fig. 8d), which is a phenotype for $T_{EFF-like}$ cells (Extended Data Fig. 8b).

To investigate whether this enhanced transition toward an effector-like state is likely related to antigen specificity, we grouped together CD8+ T cells with T cell receptors (TCRs) that share similar biophysical properties in the complementarity-determining region 3 (CDR3) (Methods), which contains the amino acids that contact antigen and MHC-I. This resulted in five TCR clusters after excluding cluster 4 due to sparsity (Extended Data Fig. 8e). For each of these TCR clusters, we next assessed how effectively member TCR clonotypes (T cells with the same TCR) transition between $T_{EFF-like}$ and T_{EX} states using a paired STARTRAC transition index (pTrans index)[35]. For TCR clusters 1 and 2, which contain among the most expanded clonotypes (Extended Data Fig. 8e,f), *Ifnar1* KO resulted in higher pTrans index values that further increased after anti-PD1 therapy (Fig. 7c). This suggested that these TCR clusters had clonotypes that more readily transition into both $T_{EFF-like}$ and T_{EX} states. Indeed, inspection of the top ten clonotypes in TCR clusters 1 and 2 from Res 499 tumors illustrated a heavily biased distribution toward the T_{EX} state that became more evenly distributed between T_{EX} and $T_{EFF-like}$ states upon *Ifnar1* KO, an effect that was further enhanced with addition of anti-PD1 therapy (Fig. 7d). Thus, preventing cancer cell IFN-I signaling enables anti-PD1 therapy to push CD8+ T cells that may otherwise become exhausted toward effector-like states in a TCR-dependent, and likely antigen-dependent, manner.

Discussion

We describe how epigenetic features of cancer cells can enhance a subset of IFN-I-related ISGs that ultimately hinder CD8+ T cell function and immunotherapy response (Fig. 7e). Our work suggests that chronic IFN-γ stimulation of cancer cells initiates epigenetic changes resembling inflammatory memory. Here, STAT1 controls active enhancers for IFN-IMDs, while IRF3 maintains their chromatin accessibility even when IFN signaling is attenuated. These primed enhancers result in greater expression of ISG.RS genes such as *OAS1* that amplifies the IFN-I pathway, augmenting expression of a compendium of genes that inhibit immune function. This restricts the generation of IFNs by immune cells, interferes with productive interactions between T cells and important DC subsets, and results in CD8+ T cells that become exhausted rather than effector like. Thus, resistant cancer cells acquire inflammatory memory domains to drive an IFN-I-mediated feedforward process that sustains feedback inhibition of immune cells. Elevated expression of ISG.RS genes represents the acquisition of inflammatory memory by cancer cells, and a decrease in IFNG.GS expression relative to ISG.RS expression represents subsequent feedback modulation of immune cells.
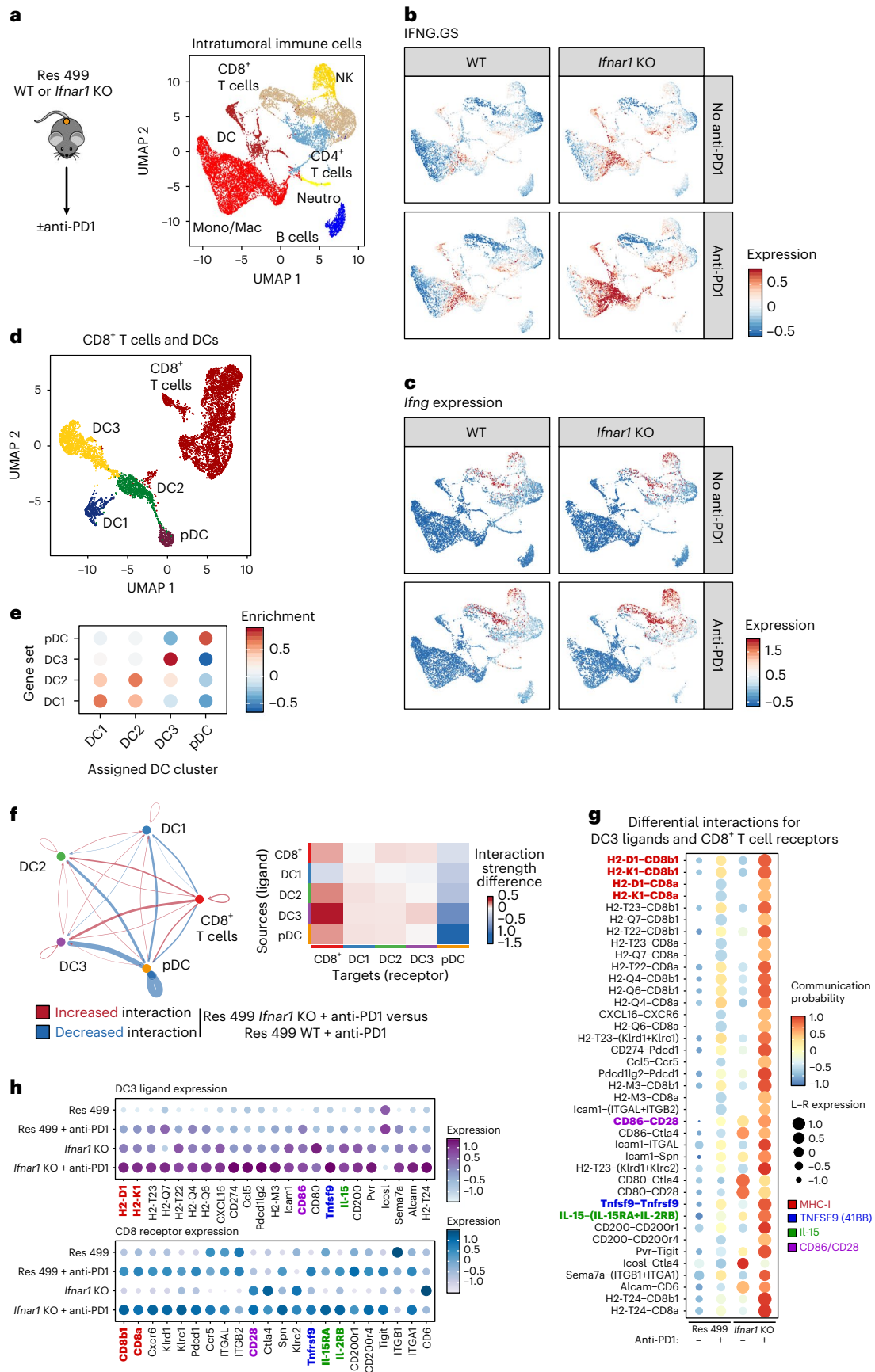
The relationship between IFN-IMDs and the ability of cancer cells to amplify IFN-I signaling has parallels with inflammatory memory in epithelial cells[25] and with trained immunity[36]. In macrophages, IFN-I and IFN-γ extensively remodel the epigenome through STATs and IRFs, leading to enhanced expression of ISGs following stimulation with TLR ligands[13,14]. In epithelial stem cells, inflammatory memory is associated with DNA-sensing PRRs[15]. We show that cancer cells that relapse after ICB amplify IFN-I signaling using the RNA sensor OAS1, which exhibits elevated expression likely due to inflammatory memory domains. These findings suggest that use of PRRs may be a common mechanism for instituting an inflammatory memory state. In Res 499 ICB-resistant tumors, STAT1 and IRF3 establish persistent chromatin accessibility both genome wide and at the *Oas1* locus. Here, chronic IFN stimulation may activate STAT1, and OAS1 or the downstream PRR RIG-I may activate IRF3 to reinforce inflammatory memory domains. Such a feedforward mechanism would then enable cancer cells to effectively use IFN-I to coordinate immune suppression despite diminished IFN-I levels resulting from immune dysfunction.
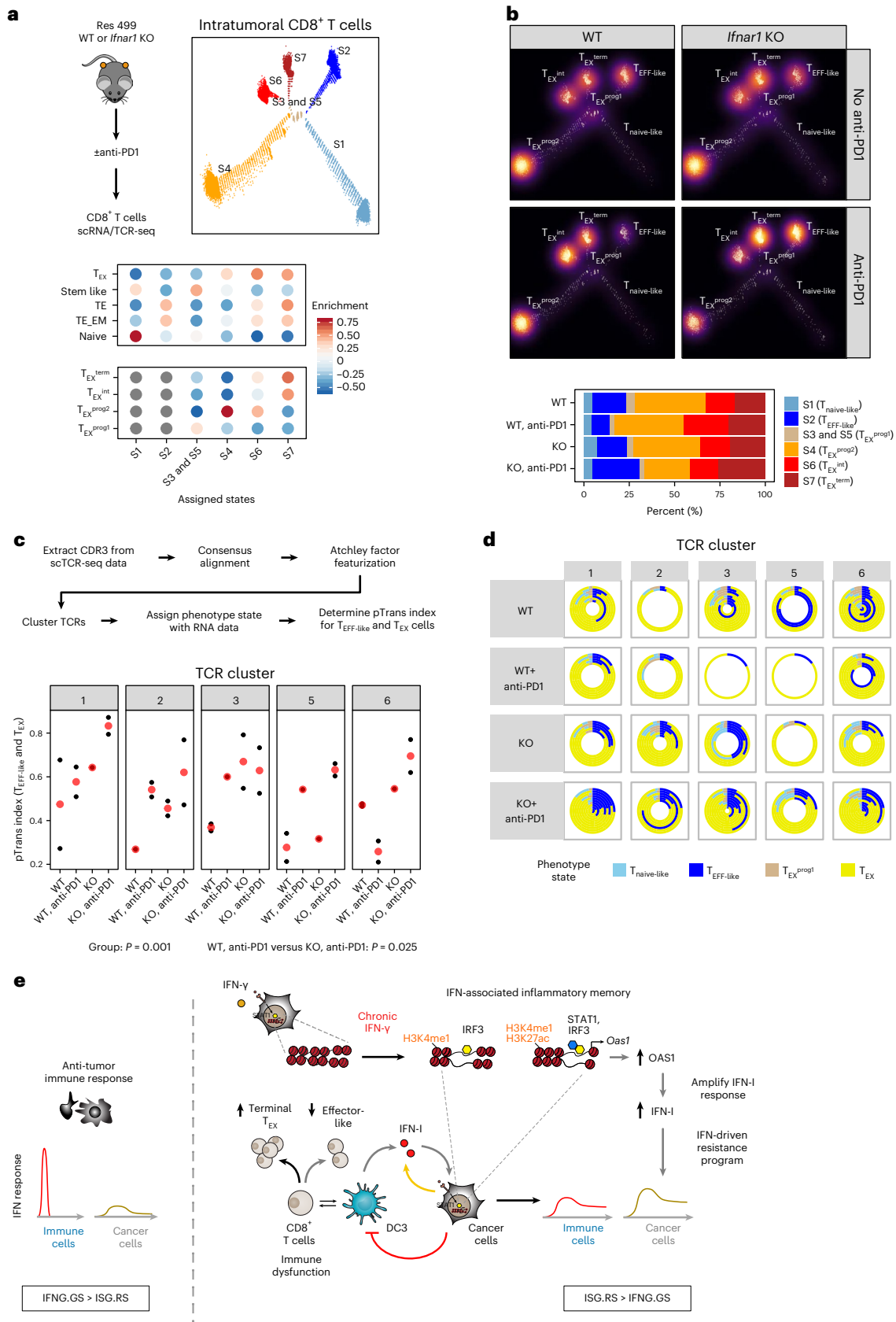
Although blocking tumor IFN-γ and IFN-I signaling both can restore the ICB response, interfering with these pathways can differ in many regards[6,7]. One key determinant for why blocking type I versus type II IFN can differ relates to the impact that each pathway can have on MHC-I expression and antigen processing. In B16 and Res 499 tumors that have low constitutive MHC-I levels but not in tumors with significantly higher baseline MHC-I levels, inhibiting IFN-γ signaling may prevent adequate MHC-I expression[7]. This impairs the ability of CD8+ T cells to recognize tumor cells but promotes innate lymphoid cell killing that rejects tumors that have lost MHC-I and/or have poor neo-antigens[7]. By contrast, inhibition of IFN-I signaling in Res 499 cells increases MHC-I likely because the IFN-γ receptor is still present on cancer cells and there is an increase in IFN-γ in the tumor due to improved immune function afforded by blocking IFN-I signaling in cancer cells. This preserves direct CD8+ T cell killing, enables durable immune

---

Fig. 6 | Inhibiting tumor IFN-I signaling enhances IFN signaling in immune cells to promote DC–CD8+ T cell interactions. a, Experimental setup and uniform manifold approximation and projection (UMAP) from scRNA-seq analysis of Res 499 tumor-infiltrating CD45+ immune cells. Cells are colored by immune cell type. Mono/Mac, monocyte or macrophage; neutro, neutrophil. **b,c**, Mean expression of IFNG.GS genes (**b**) and *Ifng* (**c**) in tumor-infiltrating CD45+ immune cells from mice bearing Res 499 control (WT) or *Ifnar1*-KO tumors treated with or without anti-PD1 therapy. **d,e**, UMAP projection of tumor-infiltrating CD8+ T cells and DC subtypes colored by immune cell type (**d**) and gene set enrichment for DC subtype gene sets (**e**) in each of the assigned DC clusters. Enrichment score is color coded. **f**, Differential cell–cell interaction strength between anti-PD1-treated Res 499 or Res 499 *Ifnar1*-KO tumors as shown by circle plot (left) and heatmap (right). Nodes in the circle plot represent DC subtypes or CD8+ T cells. Edge color represents increased or decreased interaction in treated Res 499 *Ifnar1*-KO tumors compared to treated Res 499 WT tumors. Edge width indicates the interaction strength. The heatmap shows differential interaction strengths between ligand-expressing cells (rows) and receptor-expressing cells (columns). **g,h**, Communication probability (**g**) and relative expression (**h**) of DC3 ligands and CD8+ T cell receptors from the indicated Res 499 or Res 499 *Ifnar1*-KO tumors or from the same tumors treated with anti-PD1 therapy. Select ligand–receptor (L–R) pairs are highlighted, and only ligand receptors with a communication probability of at least 20% are shown. Values are scaled.

memory, and is especially effective in combination with anti-PD1 and/ or anti-PDL1 therapy. Accordingly, as shown here and previously[6], blocking IFN signaling with a JAK inhibitor can improve ICB.

Our data suggest that preventing IFN-I signaling even in a minority of cancer cells improves ICB response. This argues that IFN-I signaling in cancer cells may prevent the generation of a factor needed to

a Res 499 WT or *Ifnar1* KO → ±anti-PD1 → CD8+ T cells scRNA/TCR-seq; Intratumoral CD8+ T cells with clusters S1–S7; Enrichment dot plots for T_EX, Stem like, TE, TE_EM, Naive and T_EX^term, T_EX^int, T_EX^prog2, T_EX^prog1 across assigned states.

b WT and *Ifnar1* KO density plots (No anti-PD1 / Anti-PD1) showing T_EX^int, T_EX^term, T_EF-like, T_EX^prog1, T_EX^prog2, T_naive-like. Bar chart of Percent (%) for WT, WT anti-PD1, KO, KO anti-PD1 with S1 (T_naive-like), S2 (T_EFF-like), S3 and S5 (T_EX^prog1), S4 (T_EX^prog2), S6 (T_EX^int), S7 (T_EX^term).

c Extract CDR3 from scTCR-seq data → Consensus alignment → Atchley factor featurization → Cluster TCRs → Assign phenotype state with RNA data → Determine pTrans index for T_EFF-like and T_EX cells. pTrans index (T_EFF-like and T_EX) across TCR clusters 1, 2, 3, 5, 6 for WT, WT anti-PD1, KO, KO anti-PD1.

Group: *P* = 0.001   WT, anti-PD1 versus KO, anti-PD1: *P* = 0.025

d TCR cluster 1, 2, 3, 5, 6 for WT, WT+anti-PD1, KO, KO+anti-PD1. Phenotype state: T_naive-like, T_EFF-like, T_EX^prog1, T_EX.

e Anti-tumor immune response; IFN response for Immune cells and Cancer cells. IFNG.GS > ISG.RS. IFN-associated inflammatory memory pathway: IFN-γ, Chronic IFN-γ, H3K4me1, IRF3, H3K4me1 H3K27ac, STAT1, IRF3, *Oas1*, ↑ OAS1, Amplify IFN-I response, ↑ IFN-I, IFN-driven resistance program. ↑ Terminal T_EX, ↓ Effector-like, CD8+ T cells, Immune dysfunction, DC3, IFN-I, Cancer cells. ISG.RS > IFNG.GS.

coordinate productive anti-tumor adaptive immunity. Consistent with this, blocking cancer cell IFN-I signaling increases IFNG.GS expression in myeloid and DC populations and is predicted to enhance interactions between CD8+ T cells and DC3 DCs. Cytokines such as CXCL9, which is

encoded by an IFNG.GS gene, can facilitate interactions between DCs and T cells[31], and increased IFN-γ produced by T cells has also been reported to allow DCs to generate IL-12 to license T cells and improve anti-PD1 efficacy[30]. Another intriguing IFN-I-regulated ISG is *Adar*,

Fig. 7 | Inhibiting tumor IFN-I signaling promotes transition of CD8+ T cell clonotypes toward an effector-like state after anti-PD1 therapy. a, Cell activation and differentiation state trajectories from scRNA-seq analysis of tumor-infiltrating CD8+ T cells (top), and gene set enrichment of genes expressed by CD8+ T cell subsets or T_{EX} cell subsets in each of the assigned T cell states (bottom). Gene set names (y axis) and T cell state labels (x axis) are shown. TE, terminal effector T cells; TE_EM, terminal effector and effector-memory T cells. States S3 and S5 were combined. **b**, Cell state trajectories (top) and frequency plot (bottom) of clonally expanded CD8+ T cells from mice with Res 499 control (WT) or Res 499 *Ifnar1*-KO tumors, treated with or without anti-PD1 therapy. Densities of cells in each labeled state are overlaid with brighter color representing a higher density. **c**, State transition potential between effector-like (S2) and exhausted T cell states (S4, S6, S7) for CD8+ T cell clonotypes from Res 499 WT or *Ifnar1*-KO (KO) tumors, treated with or without anti-PD1 therapy.

Quantitation is by a pTrans index (red dot, mean), in which higher values represent broader clonotype sharing between the two states. Clonotypes with TCRs having similar biophysical properties are clustered into one of the indicated TCR clusters. P value for differences between groups was determined by one-way ANOVA (bottom). P value for the indicated pairwise comparison was determined by Tukey's HSD test. Top, summary of the analysis approach. **d**, Distribution of T cell states (color coded) for the most expanded clonotypes belonging to each TCR cluster. The outermost ring of the concentric circles represents the most expanded clonotype with clonotypes of decreasing frequency progressing inward. Only clonotypes exceeding a frequency of 0.5% are shown, up to ten clonotypes. The T_{EX} phenotype state combines the S4, S6 and S7 exhausted T cell states. **e**, Summary of the relationship between ISG.RS and IFNG.GS with IFN-associated inflammatory memory in cancer cells, immune function, and ICB resistance. See text for details.

which restrains inflammatory signaling that can favorably shape the immune composition of tumors[37]. Thus, blocking cancer IFN-I signaling may initiate a cascade of events involving the immune TME that ultimately impacts CD8+ T cells before commitment toward terminal states. Upon treatment with anti-PD1 therapy, this may allow a greater proportion of early CD8+ T cells to differentiate toward an effector-like state rather than an exhausted state.

Methods

Mice
All animal experiments were performed according to protocols approved by the Institutional Animal Care and Use Committee and the Institutional Biosafety Committee of the University of Pennsylvania. Five- to 7-week-old female C57BL/6 (stock 027) and BALB/c (stock 28) mice were obtained from Charles River Laboratory. Five- to 7-week-old female C57BL/6 (stock 000664), *Prf1*-KO (C57BL/6-*Prf1*^{tm1Sdz}/J, stock 002407) and *Batf3*-KO (B6.129S(C)-*Batf3*^{tm1Kmm}/J, stock 013755) mice were ordered from Jackson Laboratory. Mice were maintained under specific pathogen-free conditions.

Cell lines and CRISPR gene targeting
The melanoma cell line Res 499 and the breast cancer cell line Res 237 were derived previously from B16 and TSA cells (kind gift from S. Demaria, Weill-Cornell), respectively, and cultured as previously described[16]. KO of *Ifnar1* was generated previously[6] and *Oas1a* and *Oas1g* double KO was generated using px459 with the gRNA sequence GAGGATCAGTTAAACCGACG. The targeting gRNA was annealed, phosphorylated and cloned into px459. After puromycin selection, KOs of single-cell clones were screened by treatment with 1,000 U ml^{-1} IFN-β (PBL Assay Science) and assayed for OAS1 protein expression. The double KO of *Ifnar1* and *B2m* was generated by adding an additional gRNA targeting *B2m* in *Ifnar1*-KO cells, treating cells with 100 ng ml^{-1} IFN-γ (PeproTech), and sorting KO cells on an Aria flow cytometer. The gRNA sequences for *B2m* are g1, GACAAGCACCAGAAAGACCA; g2, GTGAGTATACTTGAATTTGA.

Enzyme-linked immunosorbent assay
Cells were transfected with 0.25 µg ml^{-1} polyI:C (InvivoGen) using Lipofectamine RNAiMax (Thermo Fisher Scientific). Twenty-four hours following transfection with polyI:C, conditioned medium was collected and centrifuged to remove cells. An ELISA was carried out using the Mouse ELISA Kit (PBL Assay Science) following the manufacturer's instruction.

Real-time PCR
RNA was extracted using TRIzol, and cDNA synthesis was carried out using qScript XLT cDNA SuperMix (Quantabio) with 1 µg RNA. Real-time PCR was performed using Power SYBR Green PCR Master Mix (Applied Biosystems) on the TaqMan 7900 system (Applied Biosystems). Primer sequences for *Oas1* are as follows: forward primer, CTCCAAGGTGGTGAAGGGTG; reverse primer, TGACCCAGGACATCAAAGGC.

Small interfering RNA knockdown
SMARTPOOL ON-TARGETplus non-targeting siRNA #1, IRF1, IRF3 and IRF7 (Dharmacon) were transfected using Lipofectamine RNAiMax (Thermo Fisher Scientific) at 30 nM for 24 h before gene expression was assessed. Knockdown was confirmed by real-time PCR.

Protein expression
A western antibody against mouse OAS1 (Santa Cruz Biotechnology) was used (1:1,000 dilution). For tonic expression of OAS1, cells were plated and protein lysate was collected 24 h later. For IFN-β-stimulated expression of OAS1, cells were stimulated with 1,000 U ml^{-1} IFN-β overnight before protein lysate was collected.

In vivo mouse studies
Tumors cells were subcutaneously injected into flanks of mice. The number of cells injected were 50,000 and 100,000 for melanoma and breast cancer cells, respectively. Antibody treatments were carried out on days 5, 8 and 11 for melanoma tumors or on days 7, 10 and 13 for breast cancer tumors at 10 mg per kg (approximately 200 µg per mouse). Depletion was carried out on days −2, 0, 4, 8, 12 and 16 at 10 mg per kg, and successful depletion was confirmed by flow cytometry. Antibodies were from Bio X Cell: anti-PD1 (RMP1-14), anti-PDL1 (10F.9G2), anti-CTLA4 (9H10). Tumor volume was determined using perpendicular tumor diameters measured using calipers. Volume was calculated using the formula $L \times W^2 \times 0.52$, where L is the longest dimension and W is the perpendicular dimension. An event was defined as when tumor burden reached a protocol-specified size limit of 1.5 cm in the maximum dimension or developed skin ulceration above a protocol-specified size of 4 mm to minimize morbidity. The maximum permitted tumor burden was not exceeded. Prior power calculations using an α level of 0.05 and expected effect sizes were used to guide sample sizes for mouse studies.

Flow cytometry and cell sorting
Two weeks following tumor injection, tumors were harvested and digested with collagenase IV (EMSCO–Fisher) for 30 min at 37 °C. The suspension was filtered and treated with ACK lysis buffer (Quality Bio) for 5 min on ice. Staining was carried out first with the LIVE/DEAD Fixable Aqua Dead Cell staining kit (Thermo Fisher Scientific) and TruStain FcX (BioLegend) for 15 min at 4 °C, followed by surface antibody staining (1:50 dilution) for 30 min at 4 °C. Intracellular staining was carried out using the Foxp3/Fix/Perm kit (Thermo Fisher Scientific). Cell sorting was carried out on an LSR II or Aria flow cytometer when necessary. Fluorescently labeled anti-mouse antibodies against CD45 (104), TCR-β (H57-597), H-2Kb/H-2Db (28-8-6), I-A/I-E (M5/114.15.2), F4/80 (BM8), CD11c (N418), CD86 (GL-1), TIM3 (RMT3-23) and CX3CR1 (SA011F11) were obtained from BioLegend; those against CD8 (53-6.7),

NK1.1 (PK136), IFN-γ (XMG1.2) and perforin (eBioOMAK-D) were from eBioscience; that against CD8 (KT15) was from MBL International; that against PDL1 (MIH5) was from BD Biosciences; and those against CD11b (M1/70.15) and PD1 (J43) were from Thermo Fisher Scientific. See Supplementary Fig. 1 for representative gating strategies.

Assay for transposase-accessible chromatin and RNA sequencing

Single-cell suspensions were obtained as described above from day 15 tumors, and tumor cells were sorted by gating on live–dead aqua-negative and CD45-negative cells. A total of 50,000 or 200,000 cells were sorted for ATAC-seq or RNA-seq, respectively. RNA was extracted using Direct-zol RNA kits (Zymo Research) with on-column DNase treatment. The library was prepared using the TruSeq Stranded Total RNA Library Prep Gold kit. ATAC-seq libraries were prepared as described previously[38]. Both libraries were sequenced on the Illumina HiSeq 2500 or NextSeq 500 with 75-base paired-end reads.

Cleavage under targets and release using nuclease

For both B16 and Res 499 cells, $0.5–1 \times 10^5$ cells were collected by centrifugation (600g, 3 min, 4 °C) and washed twice with ice-cold wash buffer (20 mM HEPES-NaOH, pH 7.5; 150 mM NaCl; 0.5 mM spermidine; 1× EDTA-free protease inhibitor cocktail). The cells were resuspended in 1 ml wash buffer and incubated with 15 µl concanavalin A-coated beads (Bangs Laboratories), which were equilibrated with binding buffer (20 mM HEPES-KOH, pH 7.9; 10 mM KCl; 1 mM $CaCl_2$; 1 mM $MnCl_2$) for 10 min with rotation at room temperature. Bead-bound cells were separated by magnet and resuspended in 300 µl antibody buffer (20 mM HEPES-NaOH, pH 7.5; 150 mM NaCl; 0.5 mM spermidine; 1× EDTA-free protease inhibitor cocktail; 0.05% digitonin; 2 mM EDTA) containing 3 µg of the corresponding antibodies (anti-H3K27ac, Abcam, ab4729; anti-H3K4me1, Abcam, ab8895; anti-H3K4me3, Abcam, ab8580; rabbit IgG, Sigma-Aldrich, I8140) and incubated with rotation at 4 °C overnight. Magnetically separated beads were washed with dig-wash buffer (20 mM HEPES-NaOH, pH 7.5; 150 mM NaCl; 0.5 mM spermidine; 1× EDTA-free protease inhibitor cocktail; 0.05% digitonin) and then incubated with ~700 ng ml^{-1} pA-MNase in 300 µl dig-wash buffer at 4 °C for 1 h. After washing twice with dig-wash buffer, the beads were resuspended in 150 µl dig-wash buffer and chilled on ice for 5 min. $CaCl_2$ was added to activate MNase cleavage at a final concentration of 2 mM for 30 min. The reaction was quenched with 2× stop buffer (340 mM NaCl, 20 mM EDTA, 4 mM EGTA, 0.02% digitonin, 50 µg ml^{-1} RNase A, 50 µg ml^{-1} glycogen, 2 pg ml^{-1} heterologous spike-in DNA) at 37 °C for 15 min. The supernatant with released chromatin was collected by centrifugation, and DNA fragments were extracted using the phenol–chloroform method and used for construction of sequencing libraries.

Libraries were constructed using the NEBNext Ultra II DNA Library Prep Kit for Illumina with some modifications. For adaptor ligation, the adaptor was diluted 25-fold. For size selection of adaptor-ligated DNA, the ligation reaction was first incubated with 25 µl sparQ PureMag Beads (Quantabio) and then incubated with 45 µl beads for a second selection. For PCR amplification, the cycle number for different samples was chosen using the NEBNext Library Quant Kit for Illumina. Library concentration and size distribution was determined with the Qubit dsDNA HS Kit (Thermo) and the Bioanalyzer High Sensitivity DNA Kit (Agilent). Libraries were then sequenced using paired-end Illumina sequencing with 2 × 42-bp reads.

Statistics and reproducibility

For comparisons between two groups, the Wilcoxon test (two tailed) was used for non-parametric data, while Student's t-test (two tailed) was used for parametric data. With multiple groups, ANOVA with post hoc Tukey's HSD test was employed. The log-rank test was used for survival analysis. Normality was examined using a Shapiro–Wilk test and/or a Q–Q plot. Data collection and analysis were not typically performed blind to the conditions of the experiments. Mice were randomly assigned to each experimental group. No mice were excluded from analyses.

Integrated TCGA analysis

We downloaded the normalized ATAC-seq insertion count matrix and associated peak calls from the NCI Genomic Data Commons (https://gdc.cancer.gov/about-data/publications/ATACseq-AWG). We downloaded batch effect-normalized pan-cancer RNA-seq data from the TCGA PANCAN cohort on the UCSC Xena Browser (http://xena.ucsc.edu). To pair ATAC-seq samples with RNA-seq data, technical replicates were merged by taking the average accessibility at each peak. RNA and ATAC tumor samples were matched using converted case UUIDs. For the final paired dataset ($n = 382$), we excluded cancers of the brain (GBM, LGG) due to low immune infiltration and cancers with fewer than ten paired samples.

We inferred CD8+ T cell infiltration and activity levels through two complementary approaches. First, immune infiltration levels were inferred by CIBERSORTx. Because CIBERSORTx requires non-log data, the raw HTSeq-counts were TPM normalized for an appropriate input matrix. CIBERSORTx was run on its website (https://cibersortx.stanford.edu), using the TPM-normalized matrix as the input mixture file, the LM22 matrix as the signature gene file, 100 permutations and with quantile normalization disabled. Second, the CD8+ T cell cytolytic score was calculated for each tumor sample by taking the geometric mean of the gene expression of the CD8+ T cell-specific markers GZMA and PRF1 (ref. [23]). The CIBERSORTx-inferred CD8+ T cell infiltration level correlated strongly with the CD8+ T cell cytolytic score. We opted to use the CD8+ T cell cytolytic score as the measure of intratumoral CD8+ T cell activity.

To quantify the effect of each ISG gene set on CD8+ T cell infiltration, we employed a multiple regression model. For each cancer type, we fit a model using the modified z-score normalized gene expression of ISG.RS and IFNG.GS signatures as predictors, and the CD8+ T cell cytolytic score as the response variable.

Integrating RNA-seq and ATAC-seq data

To identify putative cis-REs for individual genes, we fit elastic net regression models using chromatin accessibility features as predictors and the RNA expression of each gene of interest as the dependent variable. For each gene of interest, we included as features all ATAC-seq peaks within a 185-kb cis-regulatory window, the median size of a mouse topological associated domain[39]. We implemented model fitting and repeated K-fold cross validation and model selection with the R package caret. Because of the small number of tumors with matched RNA-seq and ATAC-seq data, we employed an elastic net model rather than a more complicated model to reduce the risk of overfitting.

Peaks with non-zero coefficient estimates and associated with genes with a variance explained of $R^2 > 0.2$ were considered putative cis-REs. Bootstrapping peaks included in the regression model demonstrated that estimated regression coefficients are robust to random sampling. The majority of peaks had coefficient estimates of zero and were filtered out. As expected, promoter peaks (defined as −2,000 to +1,000 bp from the TSS) exhibited high coefficients, but many distal peaks upstream and downstream of TSSs also exhibited high coefficient estimates. To account for accessible peaks contributed by immune cells in the set of putative ISG.RS cis-REs, regions that overlapped with a set of known immune-specific regulatory elements[24] were filtered out.

Motif enrichment

To avoid conflating TFs with highly similar motifs, we used the 256 non-redundant archetype motifs[40] defined from clustering over 2,000 motif PWMs from the JASPAR 2018, HOCOMOCO (version 11), and Taipale 2013 databases (https://www.vierstra.org/resources/motif_clustering). We performed motif-enrichment analysis using HOMER findMotifsGenome.pl ('-size 200 -len 8,10,12,18 -mask') and the

individual motif PWMs from these databases. Significantly enriched PWMs were collapsed into archetype motifs, retaining only the most significant motif for each archetype.

ATAC-seq processing

Murine ATAC-seq data were processed using the ENCODE ATAC-seq pipeline, part of the ENCODE Uniform Processing Pipelines series (https://github.com/ENCODE-DCC/atac-seq-pipeline). In brief, adaptors were trimmed using cutadapt, and reads were aligned to the mm10 genome using Bowtie 2. After alignment, duplicate reads and reads mapping to chromosome M were removed. To correct for the Tn5 offset, BAM file reads were shifted ('+' stranded +4 bp, '−' stranded −5 bp). Peak calling was performed with MACS2, and high-confidence peaks were filtered using the irreproducible discovery rate, which selects for peaks that have consistent ranks across replicates. Overlapping peaks were merged across all conditions to generate a consensus peak set consisting of 87,697 peaks. A raw count matrix was generated by counting the number of insertions that overlapped each region in the consensus peak set. For the final count matrix, raw counts were normalized using regularized log transformation from DESeq2.

RNA-seq processing

Adaptors were trimmed with cutadapt (version 1.18). Reads were aligned to the GRCm38 genome with STAR (version 2.5.2a) using recommended parameters. Gene-based quantification was performed with salmon (version 0.13.1). For the final count matrix, raw counts were imported using tximport and normalized using regularized log transformation from DESeq2.

CUT&RUN processing

Adaptors were trimmed with cutadapt (version 1.18). Reads were aligned to the GRCm38 genome with Bowtie 2 (version 2.3.4.1) using the parameters '−local−very-sensitive-local−no-unal−no-mixed−no-discordant−phred33 -I10 -X700 -p16'. Unmapped and improperly paired reads were removed ('-F 1804 -f2'). For H3K27ac and H3K4me3 profiling, narrow peaks were called with MACS2 using the default significance threshold of $P = 1 \times 10^{-5}$. For H3K4me1 profiling, broad peaks were called using the same significance threshold. Non-overlapping, fixed-width consensus peak sets for each histone assay were generated by combining peak calls and iteratively removing overlapping peaks (only retaining the most significant peak call). A raw count matrix was generated by counting the number of insertions in each region of the consensus peak set, and normalized count matrices were generated with DESeq2's vst method.

ChromVAR

Differential TF activity was examined using chromVAR. GC bias-corrected deviations were computed from the normalized insertion count matrix generated using methods described above (see ATAC-seq processing). ChromVAR deviation values for PWMs belonging to the same Vierstra archetype motif were averaged.

Footprinting

All samples were sequenced to an average of ~60 million aligned and deduplicated reads per replicate, enough for TF footprinting. TF footprints were identified using the footprinting tool HINT-ATAC. Footprints with a low-quality score were filtered. Next, TF motifs were scanned for within footprint regions using FIMO. TFs with multiple motifs were de-deduplicated by selecting the motif with the most significant P value. To visualize TF footprints, sequence bias of Tn5 insertions was corrected for. To do this, hexamer sequences surrounding each single-base Tn5 insertion site were identified, and an observed hexamer frequency table was calculated. Next, an expected hexamer frequency table was calculated from the mm10 reference sequence. Finally, the observed-to-expected hexamer frequency ratio was calculated to generate bias-corrected Tn5 insertion counts.

Identifying interferon-associated inflammatory memory domains and genes

Inflammatory memory has previously been described as chromatin regions that gain accessibility during acute signaling, remain accessible after the signal terminus and allow for an enhanced secondary response to stimuli. We focused our analysis on 'IFN-IMDs' by terminating IFN signaling by Stat1 KO and identifying chromatin domains that uniquely maintain memory in Res 499 cells. To do this formally, we modeled chromatin accessibility in DESeq2 using the design formula '-Cell Line + Genotype + Cell Line: Genotype', where Cell Line is B16 or Res 499, Genotype is WT or Stat1 KO and the interaction term represents the cell line-specific Stat1-KO effect. We used the interaction term to filter for STAT1-dependent chromatin domains where the Stat1-KO effect is smaller for Res 499 cells than for B16 cells. We then linked these memory domains to genes that they putatively regulate by examining all genes within a 92-kb cis-regulatory window and retaining only genes that had RNA expression moderately correlated with chromatin accessibility of the linked memory domain ($r > 0.3$). The genomic features and genes are provided in Supplementary Tables 1–5.

Gene set enrichment analysis

Differential gene expression analysis was carried out using DESeq2 (version 1.24.0). GSEA was performed using fgsea (version 1.10.1).

Single-cell RNA sequencing and TCR sequencing

Tumor-infiltrating immune cells were sorted as the live–dead-negative and CD45+ population. Tumor-infiltrating CD8+ T cells were sorted as the live–dead-negative, CD45+TCR-β+CD8+ population. The sorted immune cells were loaded on a 10x Chromium Controller, and libraries were prepared using the Single Cell 5' kit and the V(D)J Mouse T Cell Enrichment kit (10x Genomics) following the manufacturer's recommendations. Libraries were sequenced on the NextSeq 500. This resulted in 3,000–4,000 cells for gene expression libraries with 25,000 reads per cell and 2,000–4,000 cells for TCR libraries with 5,000 reads per cell. Two biological replicates were sequenced, resulting in a total of 29,584 cells analyzed (Res 499, 7,692 cells; Res 499 with anti-PD1 therapy, 8,076 cells; Res 499 Ifnar1 KO, 6,758 cells; Res 499 Ifnar1 KO with anti-PD1 therapy, 7,334 cells).

Single-cell RNA-seq processing

The 10X Genomics Cell Ranger pipeline (version 3.0.0) was used to process raw data: BCL files were converted to FASTQ, reads were aligned to the mouse genome (cellranger-mm10-3.0.0) and counted, and sparse matrices were converted to dense matrices. Genes that were expressed in fewer than 0.1% of cells, cells with fewer than 500 detected genes, and cells with over 10% mitochondrial reads were removed. Gene expression was imputed using SAVER (version 1.1.2). Downstream normalization, dimensionality reduction, clustering, and integration were carried out with Seurat (version 3.1.2). Clusters (resolution = 0.15) were identified by a list of known markers for immune cells.

Gene set enrichment-score analysis

Gene sets for mouse DC subsets were published[32]. Gene sets for CD8+ T cell subsets were derived as follows: we derived a core exhaustion signature by extracting DEGs ($\log_2 > 5$, FDR > 0.01) in CD101−TIM3−, CD101−TIM3+ and CD101+TIM3+PD1+ CD8+ T cells compared to naive CD8+ T cells[41] using limma (version 3.40.6). A stem-like signature was generated by extracting DEGs ($\log_2 > 5$, FDR > 0.01) in CD101−TIM3−PD1+ compared to CD101−TIM3+ and CD101+TIM3+PD1+ and naive CD8+ T cells. The naive and effector signatures were generated using a separate RNA-seq dataset that contained naive, terminal effector (KLRG1hiCD127lo), memory precursor (KLRG1loCD127hi), central memory (CD62L+) and effector memory (CD62L−) CD8+ T cells from acute LCMV Armstrong infection and PD1+ stem-like (CXCR5+) and TIM3+ T_{EX} cells from chronic infection[41]. The naive signature was derived by extracting

genes that were expressed in naive CD8$^+$ T cells more than twofold higher than in each of the other CD8$^+$ T cell subsets. The effector signature was derived by extracting genes that are expressed more than twofold higher in effector and effector memory than in each of the other CD8$^+$ T cell subsets. We also used an effector signature generated from MC38-OVA-infiltrating CD62L$^-$SLAMF7^{hi}CX3CR1$^+$CD8$^+$ T cells[42]. Gene sets for exhausted T cell subsets were derived by extracting DEGs (log$_2$ > 1.5, FDR > 0.01) in T$_{EX}$^{prog1} (Ly108$^+$CD69$^+$), T$_{EX}$^{prog2} (Ly108$^+$CD69$^-$), T$_{EX}$^{int} (Ly108$^-$CD69$^-$) and T$_{EX}$^{term} (Ly108$^-$CD69$^+$) PD1$^+$CD8$^+$ T cells[43]. GSVA (version 1.32.0) was then used to identify enriched gene signatures for DC subsets or CD8$^+$ T cell states.

Cell–cell interaction analysis

DC and CD8$^+$ T cell interaction analysis was carried out using scTensor (version 1.0.13)[34] and with CellChat (https://github.com/sqjin/CellChat)[33]. All DCs and CD8$^+$ T cells were subsetted from intratumoral CD45$^+$ cells, and PCA analysis and cluster identification (resolution = 0.2) were carried out. CellChat and scTensor analyses were performed on DC and CD8$^+$ T cells from *Ifnar1*-KO tumors treated with anti-PD1 therapy in order to determine cell–cell interaction patterns, interaction strength, and ligand–receptor pairs.

Pseudotime analysis

Pseudotime analysis was carried out using Monocle 2 (ref. 44). Raw UMI counts from all samples were loaded as a single aggregated CellDataSet. A set of ordering genes were derived with the unsupervised dpFeature procedure from Monocle, and proliferating genes *Mki67*, *Top2a*, *Cdk1* and *Cdk2* were removed. The remaining ordering genes were used to construct pseudotime trajectories. To identify changes in T cell states after anti-PD1 treatment, TCR data were integrated. Cells that did not contain TCR information and cells that were not well expanded (clonotype frequency less than 0.2%) were removed from analysis.

Single-cell TCR-seq processing

The 10X Genomics Cell Ranger pipeline (version 2.2.0) was used to process raw data: BCL files were converted to FASTQ format, and reads were aligned to the mouse genome (cellranger-vdj-GRCm38-alts-ensemble-2.2.0) and counted. The following filtering was carried out: cells with TCRs that had undergone productive rearrangement, were full length, and contained only one TCR-α chain and one TCR-β chain were kept. Clonotypes were defined by the CDR3 amino acid sequence of the unique TCR-α and TCR-β pair, and clonotype frequency was recalculated after filtering in each biological replicate. TCR data were integrated with gene expression data by UMI. Only expanded clonotypes with a frequency exceeding 0.2% were retained for further analysis.

TCR cluster analysis

After filtering out cells that were not clonally expanded or did not contain exactly one TCR-α and one TCR-β, the amino acid sequences of the variable regions of TCR-α and TCR-β were aligned using MSA (version 1.15.0) and concatenated. The Atchley factor[45], which summarizes the physiochemical and biological properties of amino acids, was calculated for each position in TCR-α and TCR-β using HDMD (version 1.2), followed by clustering using Rphenograph (version 0.99.1) with k = 30. Assessments of clonotype sharing between state 2 (effector like) and states 4, 6, and 7 combined (exhausted) were calculated using STARTRAC pTrans index (version 0.1.0).

Reporting summary

Further information on research design is available in the Nature Portfolio Reporting Summary linked to this article.

Data availability

Raw sequencing reads and processed data for Figs. 2–4 and Extended Data Figs. 3–5 (ATAC-seq, RNA-seq, CUT&RUN) are deposited in the Gene Expression Omnibus under accession number GSE219179. Raw sequencing reads for Figs. 6 and 7 and Extended Data Figs. 7 and 8 (scRNA-seq and scTCR-seq) are deposited in the Sequence Read Archive and available under accession number PRJNA626462. RNA-seq data related to Fig. 5f have been previously deposited in the Gene Expression Omnibus under accession number GSE83850. Human RNA-seq and ATAC-seq tumor data used for Fig. 1 were derived from the TCGA Research Network and downloaded from the UCSC Xena Browser (TCGA PANCAN cohort) and the NCI Genomic Data Commons (https://gdc.cancer.gov/about-data/publications/ATACseq-AWG), respectively. Source data are provided with this paper.

Code availability

Processing and analysis code related to the TCGA and mouse integrated epigenomic analyses is deposited in a GitHub repository at https://github.com/jingyaqiu/ifnar_epigenome.

References

1. Dighe, A. S., Richards, E., Old, L. J. & Schreiber, R. D. Enhanced in vivo growth and resistance to rejection of tumor cells expressing dominant negative IFNγ receptors. *Immunity* **1**, 447–456 (1994).
2. Diamond, M. S. et al. Type I interferon is selectively required by dendritic cells for immune rejection of tumors. *J. Exp. Med.* **208**, 1989–2003 (2011).
3. Fuertes, M. B. et al. Host type I IFN signals are required for antitumor CD8$^+$ T cell responses through CD8α$^+$ dendritic cells. *J. Exp. Med.* **208**, 2005–2016 (2011).
4. Teijaro, J. R. et al. Persistent LCMV infection is controlled by blockade of type I interferon signaling. *Science* **340**, 207–211 (2013).
5. Wilson, E. B. et al. Blockade of chronic type I interferon signaling to control persistent LCMV infection. *Science* **340**, 202–207 (2013).
6. Benci, J. L. et al. Tumor interferon signaling regulates a multigenic resistance program to immune checkpoint blockade. *Cell* **167**, 1540–1554 (2016).
7. Benci, J. L. et al. Opposing functions of interferon coordinate adaptive and innate immune responses to cancer immune checkpoint blockade. *Cell* **178**, 933–948 (2019).
8. Chen, J. et al. Type I IFN protects cancer cells from CD8$^+$ T cell-mediated cytotoxicity after radiation. *J. Clin. Invest.* **129**, 4224–4238 (2019).
9. Jacquelot, N. et al. Sustained type I interferon signaling as a mechanism of resistance to PD-1 blockade. *Cell Res.* **29**, 846–861 (2019).
10. Dubrot, J. et al. In vivo CRISPR screens reveal the landscape of immune evasion pathways across cancer. *Nat. Immunol.* **23**, 1495–1506 (2022).
11. Zaretsky, J. M. et al. Mutations associated with acquired resistance to PD-1 blockade in melanoma. *N. Engl. J. Med.* **375**, 819–829 (2016).
12. Gao, J. et al. Loss of IFN-γ pathway genes in tumor cells as a mechanism of resistance to anti-CTLA-4 therapy. *Cell* **167**, 397–404 (2016).
13. Qiao, Y. et al. Synergistic activation of inflammatory cytokine genes by interferon-γ-induced chromatin remodeling and Toll-like receptor signaling. *Immunity* **39**, 454–469 (2013).
14. Park, S. H. et al. Type I interferons and the cytokine TNF cooperatively reprogram the macrophage epigenome to promote inflammatory activation. *Nat. Immunol.* **18**, 1104–1116 (2017).
15. Naik, S. et al. Inflammatory memory sensitizes skin epithelial stem cells to tissue damage. *Nature* **550**, 475–480 (2017).
16. Twyman-Saint Victor, C. et al. Radiation and dual checkpoint blockade activate non-redundant immune mechanisms in cancer. *Nature* **520**, 373–377 (2015).

17. Miller, B. C. et al. Subsets of exhausted CD8⁺ T cells differentially mediate tumor control and respond to checkpoint blockade. *Nat. Immunol.* **20**, 326–336 (2019).

18. Im, S. J. et al. Defining CD8⁺ T cells that provide the proliferative burst after PD-1 therapy. *Nature* **537**, 417–421 (2016).

19. Paley, M. A. et al. Progenitor and terminal subsets of CD8⁺ T cells cooperate to contain chronic viral infection. *Science* **338**, 1220–1225 (2012).

20. Pauken, K. E. et al. Epigenetic stability of exhausted T cells limits durability of reinvigoration by PD-1 blockade. *Science* **2807**, 1160–1165 (2016).

21. Ghoneim, H. E. et al. De novo epigenetic programs inhibit PD-1 blockade-mediated T cell rejuvenation. *Cell* **170**, 142–157 (2017).

22. Wu, T. et al. The TCF1–Bcl6 axis counteracts type I interferon to repress exhaustion and maintain T cell stemness. *Sci. Immunol.* **1**, eaai8593 (2016).

23. Rooney, M. S., Shukla, S. A., Wu, C. J., Getz, G. & Hacohen, N. Molecular and genetic properties of tumors associated with local immune cytolytic activity. *Cell* **160**, 48–61 (2015).

24. Corces, M. R. et al. The chromatin accessibility landscape of primary human cancers. *Science* **362**, eaav1898 (2018).

25. Larsen, S. B. et al. Establishment, maintenance, and recall of inflammatory memory. *Cell Stem Cell* **28**, 1758–1774 (2021).

26. Ordovas-Montanes, J., Beyaz, S., Rakoff-Nahoum, S. & Shalek, A. K. Distribution and storage of inflammatory memory in barrier tissues. *Nat. Rev. Immunol.* **20**, 308–320 (2020).

27. Malathi, K., Dong, B., Gale, M. & Silverman, R. H. Small self-RNA generated by RNase L amplifies antiviral innate immunity. *Nature* **448**, 816–819 (2007).

28. Hornung, V., Hartmann, R., Ablasser, A. & Hopfner, K. P. OAS proteins and cGAS: unifying concepts in sensing and responding to cytosolic nucleic acids. *Nat. Rev. Immunol.* **14**, 521–528 (2014).

29. Manguso, R. T. et al. In vivo CRISPR screening identifies Ptpn2 as a cancer immunotherapy target. *Nature* **547**, 413–418 (2017).

30. Garris, C. S. et al. Successful anti-PD-1 cancer immunotherapy requires T cell–dendritic cell crosstalk involving the cytokines IFN-γ and IL-12. *Immunity* **49**, 1148–1161 (2018).

31. Chow, M. T. et al. Intratumoral activity of the CXCR3 chemokine system is required for the efficacy of anti-PD-1 therapy. *Immunity* **50**, 1498–1512 (2019).

32. Zilionis, R. et al. Single-cell transcriptomics of human and mouse lung cancers reveals conserved myeloid populations across individuals and species. *Immunity* **50**, 1317–1334 (2019).

33. Jin, S. et al. Inference and analysis of cell–cell communication using CellChat. *Nat. Commun.* **12**, 1088 (2021).

34. Tsuyuzaki, K., Ishii, M. & Nikaido, I. Uncovering hypergraphs of cell–cell interaction from single cell RNA-sequencing data. Preprint at *bioRxiv* https://doi.org/10.1101/566182 (2019).

35. Zhang, L. et al. Lineage tracking reveals dynamic relationships of T cells in colorectal cancer. *Nature* **564**, 268–272 (2018).

36. Netea, M. G. et al. Trained immunity: a program of innate immune memory in health and disease. *Science* **352**, aaf1098 (2016).

37. Ishizuka, J. J. et al. Loss of ADAR1 in tumours overcomes resistance to immune checkpoint blockade. *Nature* **565**, 43–48 (2019).

38. Buenrostro, J. D., Wu, B., Chang, H. Y. & Greenleaf, W. J. ATAC-seq: a method for assaying chromatin accessibility genome-wide. *Curr. Protoc. Mol. Biol.* **2015**, 21.29.1–21.29.9 (2015).

39. Rao, S. S. et al. A 3D map of the human genome at kilobase resolution reveals principles of chromatin looping. *Cell* **159**, 1665–1680 (2014).

40. Vierstra, J. et al. Global reference mapping of human transcription factor footprints. *Nature* **583**, 729–736 (2020).

41. Hudson, W. H. et al. Proliferating transitory T cells with an effector-like transcriptional signature emerge from PD-1⁺ stem-like CD8⁺ T cells during chronic infection. *Immunity* **51**, 1043–1058 (2019).

42. Kurtulus, S. et al. Checkpoint blockade immunotherapy induces dynamic changes in PD-1⁻CD8⁺ tumor-infiltrating T cells. *Immunity* **50**, 181–194 (2019).

43. Beltra, J. C. et al. Developmental relationships of four exhausted CD8⁺ T cell subsets reveals underlying transcriptional and epigenetic landscape control mechanisms. *Immunity* **52**, 825–841 (2020).

44. Trapnell, C. et al. The dynamics and regulators of cell fate decisions are revealed by pseudotemporal ordering of single cells. *Nat. Biotechnol.* **32**, 381–386 (2014).

45. Atchley, W. R., Zhao, J., Fernandes, A. D. & Drüke, T. Solving the protein sequence metric problem. *Proc. Natl Acad. Sci. USA* **102**, 6395–6400 (2005).

Author contributions

J.Q., B.X. and A.J.M. designed experiments. B.X. performed the main experiments; D.R., S.W. and J.S. assisted with epigenome profiling; and J.L.B., Y.X. and D.Y. assisted with mouse and immune profiling studies. J.Q. and A.J.M. designed computational methods. J.Q., B.X. and A.J.M. analyzed data, interpreted results and wrote the manuscript. H.I. assisted with computation methods. J.-C.B. provided data for exhausted T cell subsets. J.-C.B. and E.J.W. assisted in the interpretation of T cell exhaustion studies. A.J.M. oversaw the study.

Competing interests

A.J.M. is a project member of the Parker Institute for Cancer Immunotherapy and has received research funding from Merck. He has also received honoraria and travel support from Merck, AstraZeneca and Pfizer. He is a scientific founder for Dispatch Biotherapeutics and a scientific consultant for Takeda, Xilio, H3 Biomedicine and Related Sciences. A.J.M. is an inventor on patents related to the IFN pathway and is on a filed patent related to modified CAR T cells. J.L.B. is currently an employee of Bristol Myers Squibb. Y.X. is a current employee of Pfizer. B.X. is currently an employee of Incyte. E.J.W. is a member of the Parker Institute for Cancer Immunotherapy and has consulting agreements with and/or is on the scientific advisory board for Merck, Roche, Pieris, Elstar and Surface Oncology. E.J.W. has a patent licensing agreement on the PD1 pathway with Roche–Genentech and is a founder of Arsenal Biosciences. The remaining authors declare no relevant competing interests.

Additional information

Extended data is available for this paper at https://doi.org/10.1038/s43018-022-00490-y.

Supplementary information The online version contains supplementary material available at https://doi.org/10.1038/s43018-022-00490-y.

Correspondence and requests for materials should be addressed to Andy J. Minn.
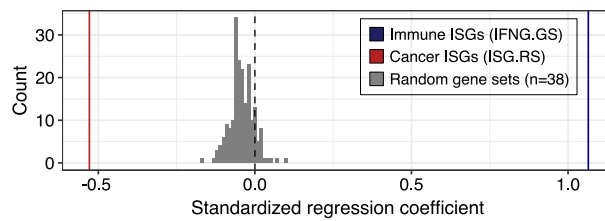
A

Interrogating relationship between ISG.RS expression, cancer cell epigenetics, and CD8 immune activity
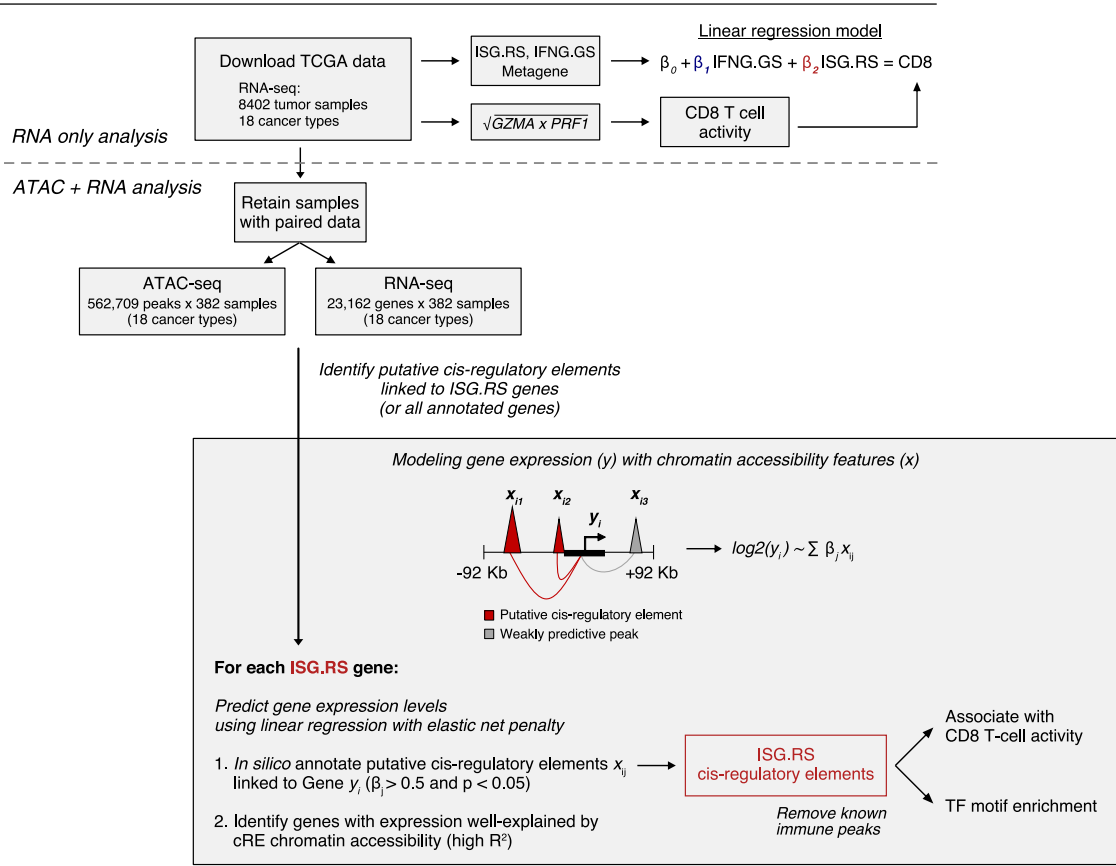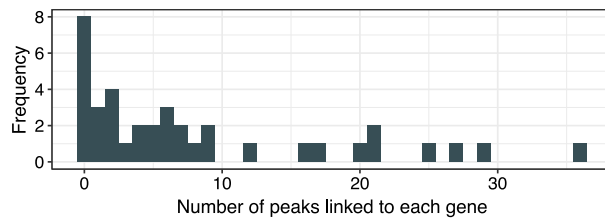

B
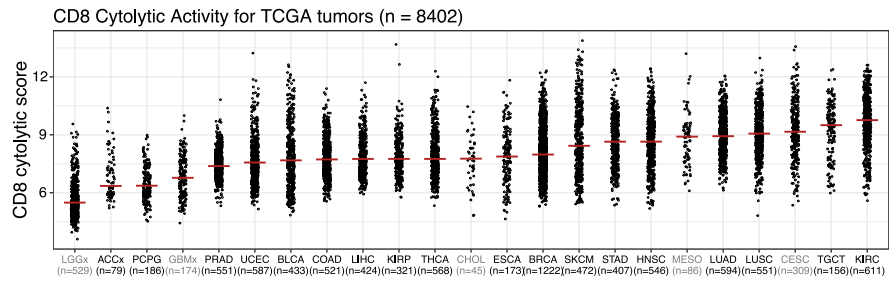
C

D

**Extended Data Fig. 1 | See next page for caption.**

Extended Data Fig. 1 | Relationship between ISGs and T cell activity in TCGA tumors. A. Schematic depicting the datasets and strategy used for the integrated analysis of RNA-seq and ATAC-seq data from TCGA tumor samples. **B**. CD8 T cell cytolytic activity scores (CD8 cytolytic activity) for all TCGA tumors, ordered by increasing median score (red line) for each cancer type. Cancer types with grey labels were excluded from analysis due to known low immune infiltration or low numbers of samples with paired RNA and ATAC data. **C**. Standardized regression coefficient estimates representing the effect of modified Z-score normalized RNA expression of IFNG.GS, ISG.RS, or 250 random gene sets (n = 38, same size as ISG.RS gene set) on CD8 T cell cytolytic activity. **D**. Histogram of number of putative cis-regulatory elements linked to each ISG.RS gene.
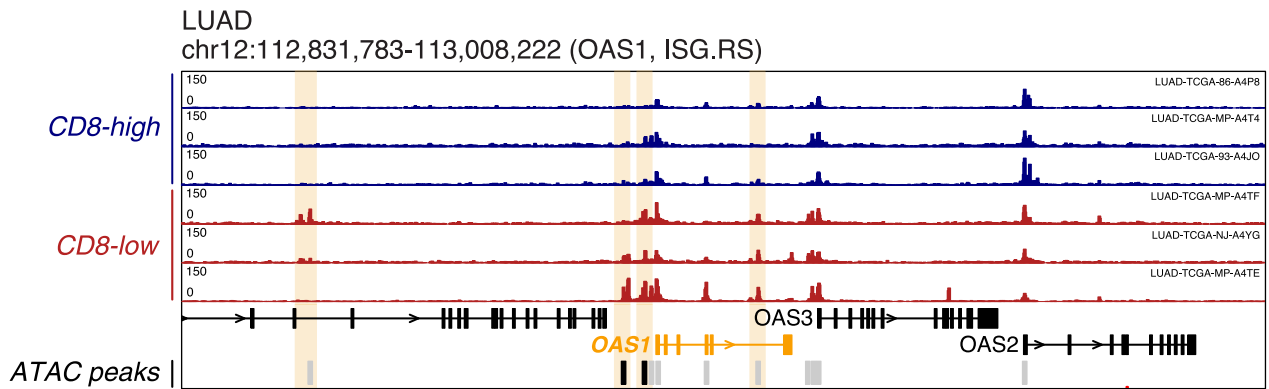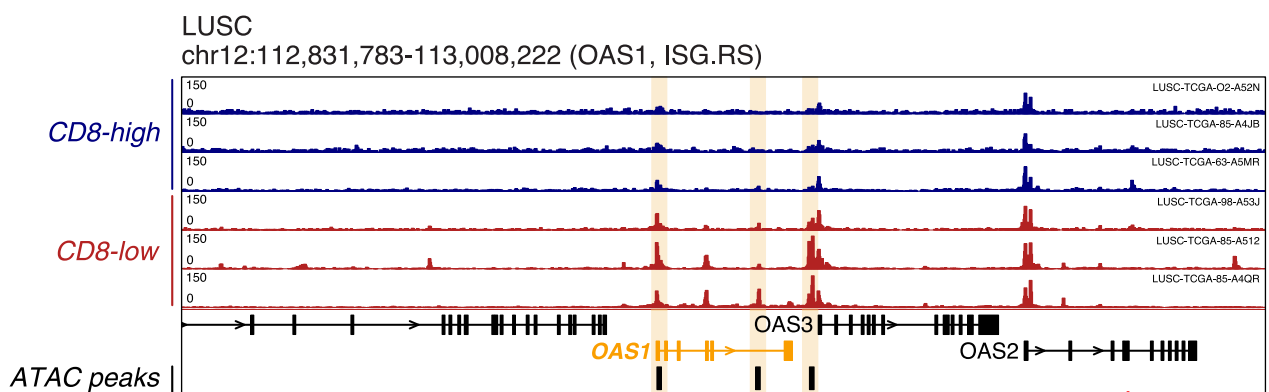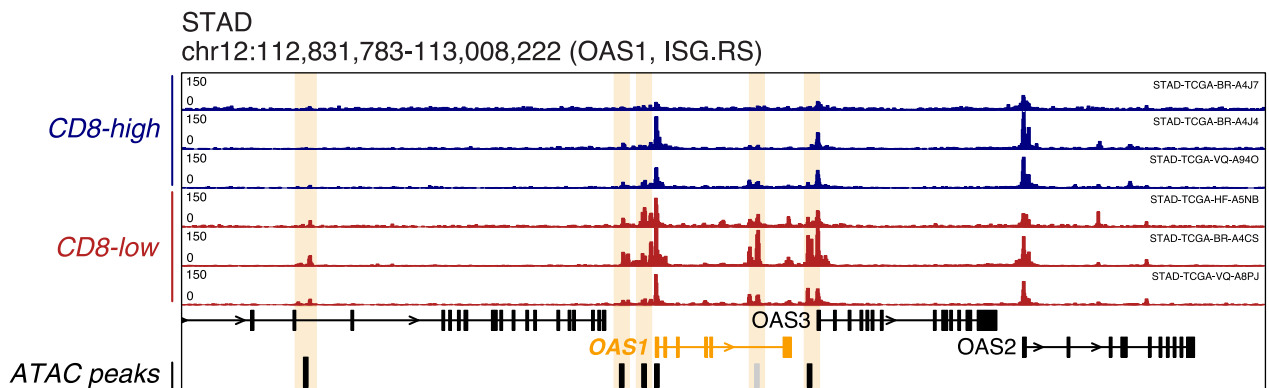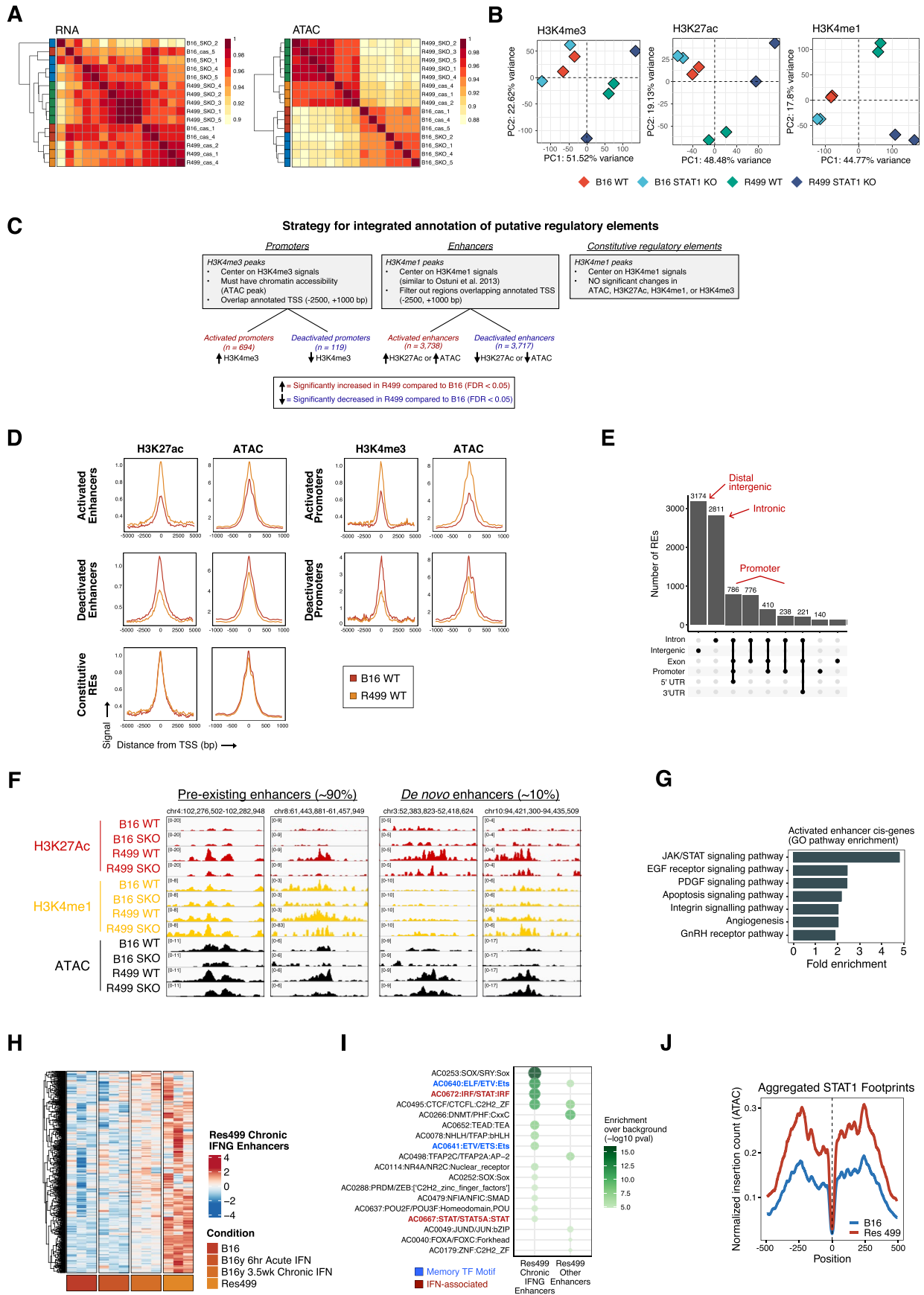
Extended Data Fig. 2 | *OAS1* cis-regulatory elements in TCGA tumors. A-C. ATAC tracks at the *OAS1* loci for representative LUAD, LUSC, and STAD tumors with high (blue) or low (red) CD8 T cell cytolytic activity. The annotation bar (bottom) demarcates called peaks, with black and grey bars indicating putative cis-REs linked to *OAS1* and other peaks in the region, respectively. Highlighted peaks indicate putative cis-REs that negatively correlate with CD8 T cell cytolytic activity. The correlation of average *OAS1* cis-RE chromatin accessibility with CD8 T cell cytolytic activity across all paired tumor samples available for each cancer type is depicted in Fig. 1i.

A RNA ATAC

B H3K4me3 H3K27ac H3K4me1

B16 WT   B16 STAT1 KO   R499 WT   R499 STAT1 KO

C Strategy for integrated annotation of putative regulatory elements

Promoters

H3K4me3 peaks
• Center on H3K4me3 signals
• Must have chromatin accessibility (ATAC peak)
• Overlap annotated TSS (-2500, +1000 bp)

Activated promoters (n = 694) ↑H3K4me3
Deactivated promoters (n = 119) ↓H3K4me3

Enhancers

H3K4me1 peaks
• Center on H3K4me1 signals (similar to Ostuni et al. 2013)
• Filter out regions overlapping annotated TSS (-2500, +1000 bp)

Activated enhancers (n = 3,738) ↑H3K27Ac or ↑ATAC
Deactivated enhancers (n = 3,717) ↓H3K27Ac or ↓ATAC

Constitutive regulatory elements

H3K4me1 peaks
• Center on H3K4me1 signals
• NO significant changes in ATAC, H3K27Ac, H3K4me1, or H3K4me3

↑ = Significantly increased in R499 compared to B16 (FDR < 0.05)
↓ = Significantly decreased in R499 compared to B16 (FDR < 0.05)

D H3K27ac ATAC H3K4me3 ATAC

Activated Enhancers
Activated Promoters
Deactivated Enhancers
Deactivated Promoters
Constitutive REs

Signal

Distance from TSS (bp) →

B16 WT
R499 WT

E Number of REs

Distal intergenic
Intronic
Promoter

3174 2811 786 776 410 238 221 140

Intron
Intergenic
Exon
Promoter
5' UTR
3'UTR

F Pre-existing enhancers (~90%) *De novo* enhancers (~10%)

H3K27Ac
B16 WT
B16 SKO
R499 WT
R499 SKO

H3K4me1
B16 WT
B16 SKO
R499 WT
R499 SKO

ATAC
B16 WT
B16 SKO
R499 WT
R499 SKO

G Activated enhancer cis-genes (GO pathway enrichment)

JAK/STAT signaling pathway
EGF receptor signaling pathway
PDGF signaling pathway
Apoptosis signaling pathway
Integrin signaling pathway
Angiogenesis
GnRH receptor pathway

Fold enrichment

H

Res499 Chronic IFNG Enhancers

Condition
B16
B16γ 6hr Acute IFN
B16γ 3.5wk Chronic IFN
Res499

I

AC0253:SOX/SRY:Sox
AC0640:ELF/ETV:Ets
AC0672:IRF/STAT:IRF
AC0495:CTCF/CTCFL:C2H2_ZF
AC0266:DNMT/PHF:CxxC
AC0652:TEAD:TEA
AC0078:NHLH/TFAP:bHLH
AC0641:ETV/ETS:Ets
AC0498:TFAP2C/TFAP2A:AP-2
AC0114:NR4A/NR2C:Nuclear_receptor
AC0252:SOX:Sox
AC0288:PRDM/ZEB:['C2H2_zinc_finger_factors']
AC0479:NFIA/NFIC:SMAD
AC0637:POU2F/POU3F:Homeodomain,POU
AC0667:STAT/STAT5A:STAT
AC0049:JUND/JUN:bZIP
AC0040:FOXA/FOXC:Forkhead
AC0179:ZNF:C2H2_ZF

Enrichment over background (−log10 pval)
15.0
12.5
10.0
7.5
5.0

Res499 Chronic IFNG Enhancers
Res499 Other Enhancers

Memory TF Motif
IFN-associated

J Aggregated STAT1 Footprints

Normalized insertion count (ATAC)

Position

B16
Res 499

Extended Data Fig. 3 | See next page for caption.

Extended Data Fig. 3 | Activated enhancers in ICB-resistant cancer cells.
A. Spearman pairwise correlation of RNA and ATAC libraries. Heatmap is
hierarchically clustered. **B**. PCA of H3K4me3, H3K27ac, and H3K4me1 signals for
B16 and Res 499 cells with or without *Stat1* knockout (SKO) sorted from *in vivo*
tumors (n = 2 mice per group). **C**. Strategy for integrated annotation of putative
regulatory elements. **D**. Summary profiles of H3K4me3, H3K27ac, and ATAC
signal intensity over activated or deactivated promoters and enhancers (n = 2
mice per condition for H3K4me3 and H3K27ac assays; n = 5 mice per condition
for ATAC assay). **E**. Genomic regions where Res 499 activated or deactivated
regulatory elements reside. Only regulatory elements with significant
differences in H3K27ac, H3K4me3, or ATAC signal intensity are included
(FDR < 0.05). **F**. Example tracks for activated enhancers in Res 499 that are either
pre-existing (left) or *de novo* activated (right). **G**. Enriched PANTHER pathways
for genes located within a 50 Kb cis-regulatory window of Res 499 activated

enhancers. P-values determined by Fisher's exact test and FDR calculated
by the Benjamini-Hochberg procedure. All pathways shown are significant
with FDR < 0.01. **H**. Chromatin accessibility of the subset of Res 499 activated
enhancers induced by chronic IFNG signaling (900 out of 3,738 enhancers) in
cancer cells sorted from the indicated *in vivo* tumors (n = 3 mice per condition),
where each row represents a chronic IFNG-induced enhancer. Summary
enrichment scores for these loci are shown in Fig. 2i. B16 tumors were treated
with IFNG *in vitro* for 6 hours (acute) or 3.5 weeks (chronic) prior to implantation
into syngeneic mice. **I**. Enrichment of archetype motifs in Res 499 activated
enhancers that are chronic IFNG-induced or not. P-values are color-coded and
larger circle sizes indicate greater significance. TF motifs highlighted in red
are associated with IFN signaling, TF motifs highlighted in blue are associated
with inflammatory memory. **J.** Normalized ATAC-seq insertion counts at DNA
footprints with ISRE motifs in B16 or Res 499 cells.
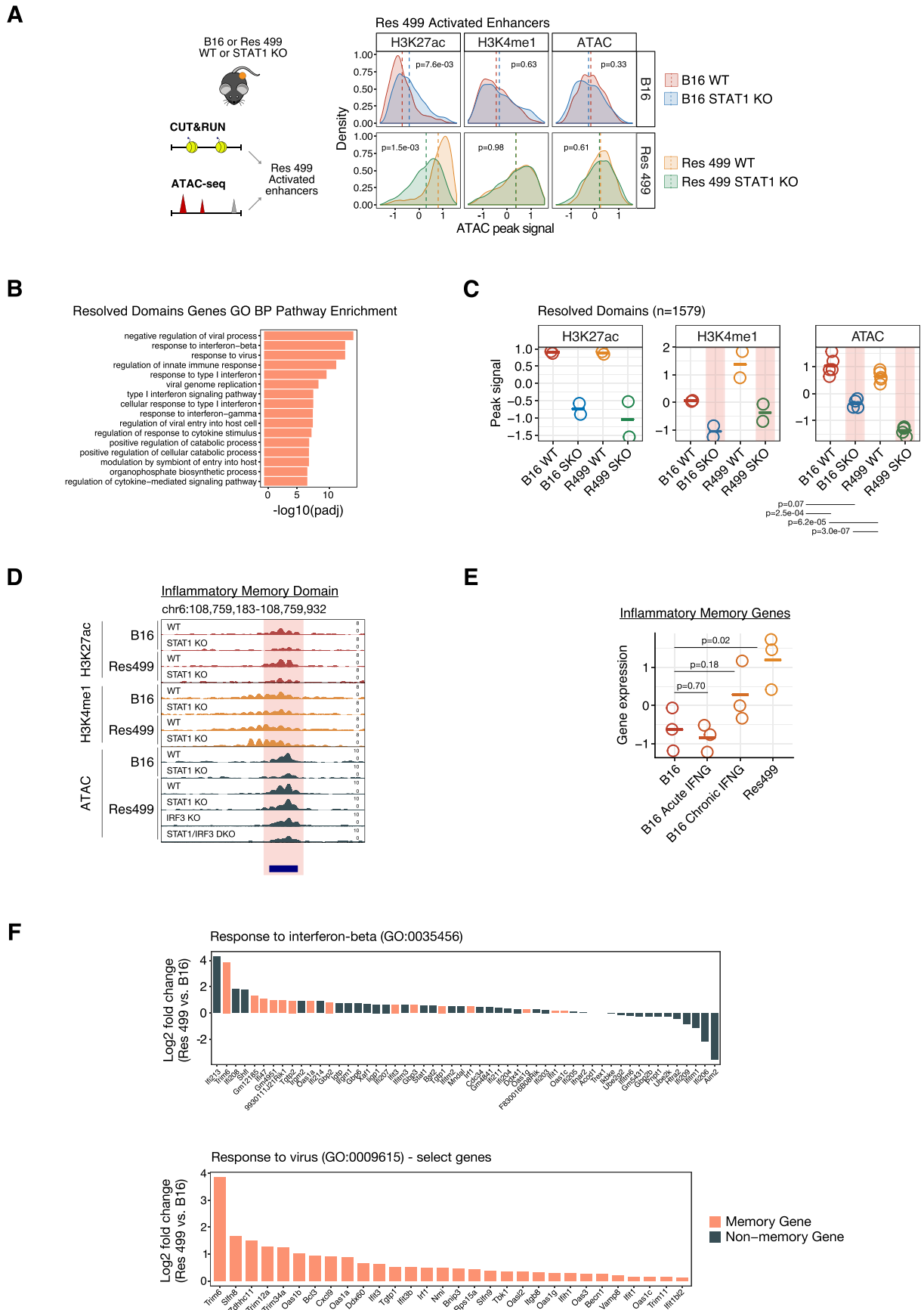
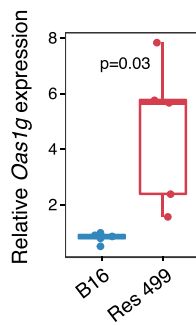Extended Data Fig. 4 | See next page for caption.

Extended Data Fig. 4 | Features of IFN-associated inflammatory memory and resolved domains. A. Density histogram representing the distribution of H3K27ac, H3K4me1, or ATAC signal intensity at individual Res 499 activated enhancers in cancer cells from B16 or Res 499 WT or *Stat1* KO tumors. Dotted line indicates the mean signal intensity of all activated enhancers for the specified condition. P-values determined using the summary enrichment scores for each condition, and a one-way ANOVA with post-hoc Tukey HSD to calculate significance of pairwise comparisons. **B**. Top GO Biological Processes terms enriched in genes linked to resolved domains. **C**. Summary enrichment scores of H3K27ac, H3K4me1, or ATAC signal at resolved domains in cancer cells sorted from the indicated *in vivo* tumors (n = 2 mice per condition for H3K27ac and H3K4me1 assays; n = 5 mice per condition for ATAC assay). **D**. Representative track for H3K27ac, H3K4me1, and ATAC signal at an IFN-associated inflammatory memory domain (IFN-IMD) (more examples shown in Fig. 3c). Red bars highlight the IFN-IMD domain where persistent memory features specific to Res 499 tumors are revealed by *Stat1* KO. **E**. Summary gene set enrichment scores for the IFN-associated inflammatory memory gene signature from cancer cells sorted from the indicated *in vivo* tumors. B16 tumors were treated with IFNG *in vitro* for 6 hours (acute) or 3.5 weeks (chronic) prior to implantation into syngeneic mice (n = 3 mice per condition). P-values determined by two-sided t-test. **F**. Log2 fold change in RNA expression between Res 499 and B16 tumors for individual genes in the specified gene set. Coral color indicates an inflammatory memory gene that is summarized in Fig. 3f.
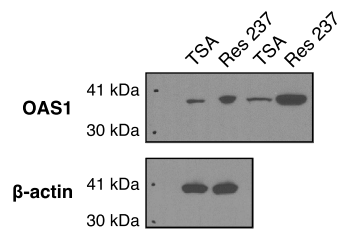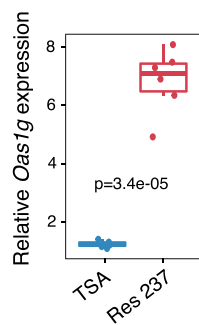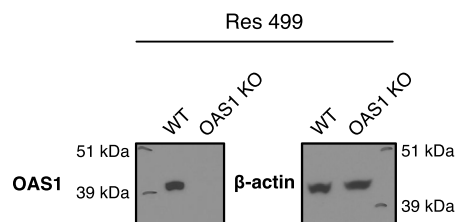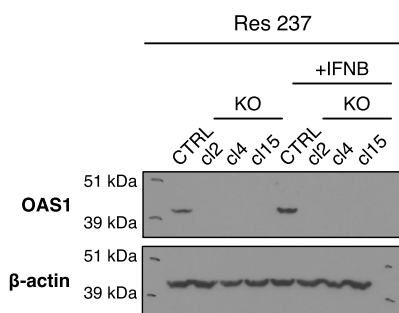
A

Res 499 Intratumoral Immune Cells
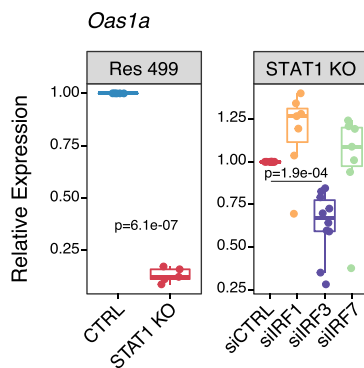
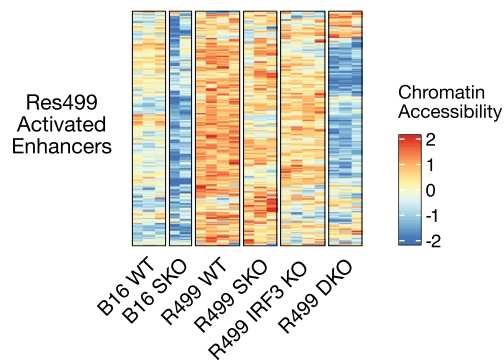**B**

C

D

E

F

G

Type I IFN

H

Oas1a
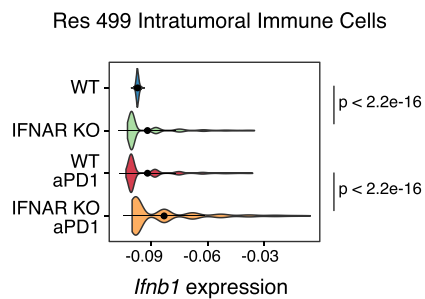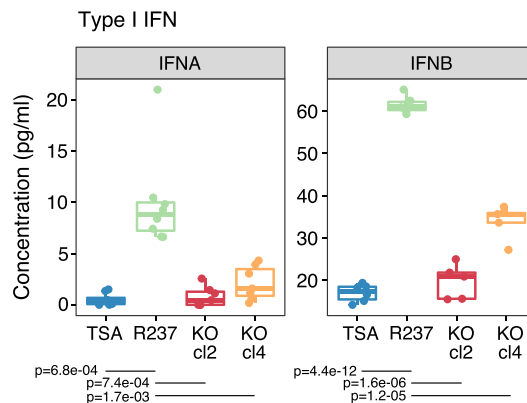
I

Extended Data Fig. 5 | See next page for caption.

Extended Data Fig. 5 | OAS1 regulates IFN-I signaling and IRF3 maintains accessibility of activated enhancers in ICB-resistant cancer cells. A. *Ifnb* expression in tumor infiltrating CD45⁺ immune cells from mice with Res 499 WT or *Ifnar1* KO (IFNAR KO) tumors, treated with or without anti-PD1 (n = 29,584 cells from 2 biological replicates per condition). P-values determined by two-sided Wilcoxon test. **B**. RNA expression of OAS1 in B16 and Res 499 cells *in vitro* (n = 5 per condition). P-values determined by two-sided t-test. **C-D**. Protein **(C)** and RNA **(D)** expression of OAS1 in TSA and ICB-resistant Res 237 breast cancer cells *in vitro* (RNA, n = 6 per group). Replicate samples are shown in the protein blot. P-values determined by two-sided t-test. **E**. Protein expression of OAS1 in Res 499 WT and *Oas1* KO cells. Shown is representative of two technical repeats. **F**. Protein expression of OAS1 following IFNB (1000 U/ml) stimulation in Res 237 control

(CTRL) and Res 237 *Oas1* KO clones (cl2, 4, 15). Shown is representative of two technical repeats. **G**. Concentration of IFNA and IFNB after polyI:C transfection of TSA, Res 237 (R237), and Res 237 *Oas1* KO clones (cl2, cl4) (TSA, n = 8; Res 237, n = 8; cl2, n = 7; cl4, n = 4 biological replicates). P-values determined by two-sided t-test. **H**. *Oas1* expression in Res 499 control (CTRL) or Res 499 *Stat1* KO cells *in vitro* (left; Res 499 CTRL, n = 10; Res 499 *Stat1* KO) or in Res 499 *Stat1* KO cells following siRNA knockdown of control RNA (siCTRL) or the indicated IRFs (right; n = 10; siCTRL, n = 10; siIRF1, n = 7; siIRF3, n = 10, siIRF7, n = 7, siIRF9, n = 7). P-values determined by two-sided t-test. **I**. Chromatin accessibility of individual Res 499 activated enhancers in cancer cells sorted from the indicated *in vivo* tumors. Boxplots represent the 25ᵗʰ percentile, median, 75ᵗʰ percentile, and 1.5x IQR (whiskers).
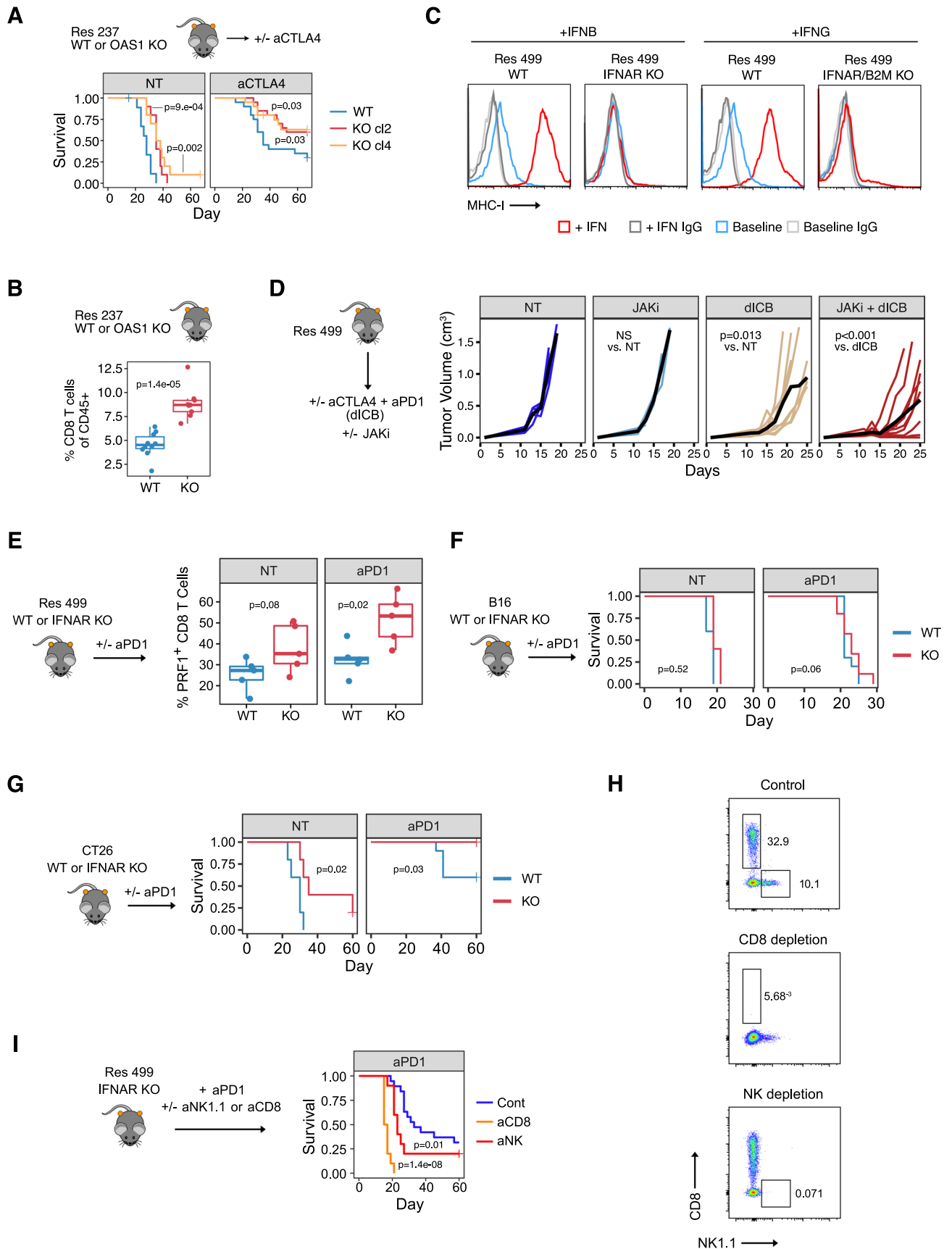
Extended Data Fig. 6 | See next page for caption.

Extended Data Fig. 6 | Blocking cancer cell IFN-I signaling increases the frequency of tumor-infiltrating CD8 T cells and improves ICB response. A. Survival of mice with Res 237 WT or *Oas1* KO (KO) tumors either non-treated (NT) or treated with anti-CTLA4 (aCTLA4) (NT, n = 10 mice per condition; aCTLA4, n = 20 mice per condition). Two independent KO clones are shown. P-values determined by two-sided log-rank test. **B**. Percent of tumor infiltrating CD8 T cells in total CD45⁺ cells from mice with Res 237 WT or Res 237 *Oas1* KO (KO) tumors. P-values determined by two-sided t-test. **C**. MHC-I surface expression at baseline and after either IFNB or IFNG treatment of the indicated cell lines to assess knockout of *B2m* and/or *Ifnar1* in Res 499 cancer cells. **D**. Tumor volume growth of mice injected with Res 499 tumors and treated with anti-CTLA4 plus anti-PD1 (dICB), delayed administration of the JAK inhibitor ruxolitinib (JAKi),

or both (NT and JAKi, n = 5 mice per condition; dICB and JAKi + dICB, n = 10 mice per condition). P-values determined by a mix-effect regression model. **E**. Percent of PRF1⁺ CD8 T cells relative to total CD8 T cells in Res 499 WT or Res 499 *Ifnar1* KO (KO) tumors from mice treated with or without anti-PD1 (aPD1) (n = 5 mice per group). P-values determined by two-sided t-test. **F-G**. Survival of mice with B16 WT or *Ifnar1* KO (KO) tumors (**F**), or CT26 WT or *Ifnar1* KO (KO) tumors (**G**), either non-treated (NT) or treated with anti-PD1 (NT, n = 5 mice per condition; aPD1, n = 10 mice per condition). P-values determined by two-sided log-rank test. **H**. Representative density plot of peripheral CD45⁺ cells in control mice or mice treated with anti-CD8 or anti-NK1.1 depleting antibody. **I**. Data shown in Fig. 5a replotted to emphasize effect of host immune cell status. Boxplots represent the 25th percentile, median, 75th percentile, and 1.5x IQR (whiskers).
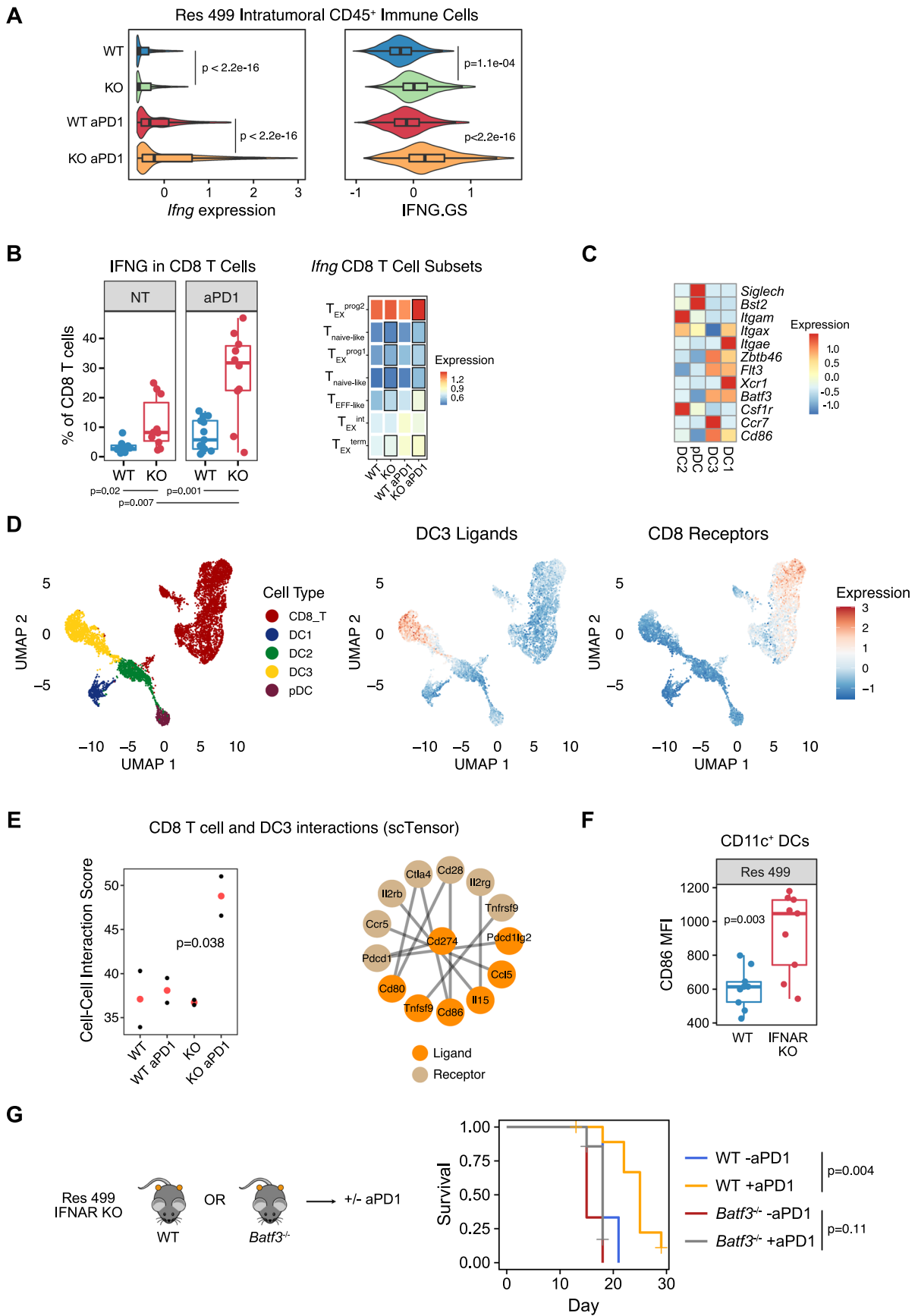
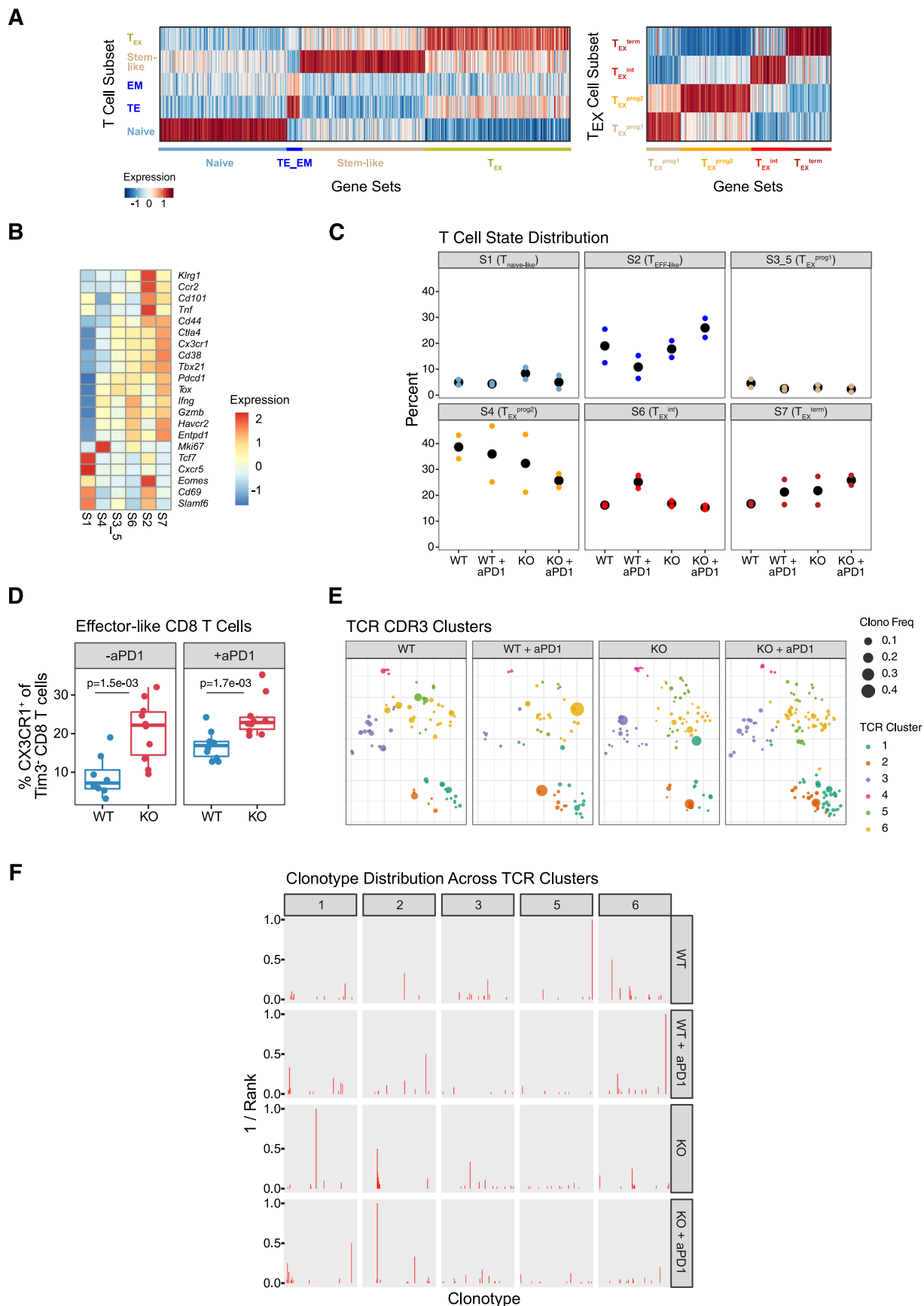**Extended Data Fig. 7 | See next page for caption.**

Extended Data Fig. 7 | Blocking cancer cell IFN-I signaling improves immune cell IFNG signaling and predicted interactions between DCs and CD8 T cells. A. Distribution of *Ifng* and IFNG.GS expression in tumor infiltrating CD45⁺ immune cells from mice with Res 499 WT or *Ifnar1* KO (KO) tumors treated with or without anti-PD1 (aPD1) (n = 29,584 cells from 2 biological replicates per condition). P-values determined by two-sided Wilcoxon test. **B**. Percent CD8 T cells expressing IFNG by flow cytometry (left; n = 13 mice per group) or average expression of *Ifng* in CD8 T cell subsets by scRNA-seq (right) from the indicated tumors either non-treated (NT) or treated with anti-PD1. P-values determined by two-sided t-test. For heatmap of *Ifng* expression, boxed values in second column indicate p < 0.05 for comparison between WT vs. *Ifnar1* KO, and boxed values in fourth column are for WT + aPD1 vs. *Ifnar1* KO + aPD1. **C**. Average expression of select markers for indicated DC subtype clusters shown in Fig. 6d. **D**. Average

expression of DC3 ligands and CD8 T cell receptors from the receptor-ligands shown in Fig. 6h. The cell types are annotated in the UMAP on the left. **E**. Cell-cell interaction scores (left) and ligand-receptor interactions (right) between CD8 T cells and DC3 using *scTensor*. Data are from mice bearing Res 499 WT or *Ifnar1* KO tumors treated with or without anti-PD1. Cell-cell interaction scores and the mean (red dot) are from biological replicates. P-value determined by a one-way ANOVA for differences between groups. **F**. Surface expression of CD86 on MHC-II⁺ CD11c⁺ DCs from Res 499 WT or *Ifnar1* KO tumors (n = 9 per condition). P-values determined by two-sided t-test. **G**. Survival of wildtype (WT) or *Batf3*⁻/⁻ mice with Res 499 *Ifnar1* KO cells treated with or without anti-PD1 (WT mice NT, n = 5; WT mice aPD1, n = 10; *Batf3* -/- mice NT, n = 3; *Batf* -/- mice aPD1, n = 7). P-values determined by two-sided log-rank test. Boxplots represent the 25ᵗʰ percentile, median, 75ᵗʰ percentile, and 1.5x IQR (whiskers).

Extended Data Fig. 8 | See next page for caption.

Extended Data Fig. 8 | Blocking cancer cell IFN-I signaling alters features of tumor-infiltrating CD8 T cells. A-B. Expression of CD8 T cell gene sets **(A)** and average expression of select markers **(B)** used to annotate CD8 T cell states shown in Fig. 7a. **C.** Percentage CD8 T cells occupying each state for each biological replicate (n = 2 mice per condition). Black dot represents mean. **D**. Percent of CX3CR1[+] effector-like T cells relative to TIM3^{-} CD8 T cells in Res 499 WT or Res 499 *Ifnar1* KO (KO) tumors from mice treated with or without anti-PD1 (aPD1) (n = 10 mice per condition). **E-F**. UMAP of CD8 T cell clonotypes clustered by biophysical features of TCR CDR3 amino acids **(E)** and the distribution of expanded T cell clonotypes across TCR clusters **(F)** in Res 499 WT or Res 499 *Ifnar1* KO (KO) tumors from mice treated with or without anti-PD1. In the UMAP, TCR clusters are color-coded and circle size indicates clonotype frequency. In the bar plot, each bar is one unique clonotype stratified by TCR cluster, with the height of the bar representing the reciprocal of the rank order by clonotype frequency (higher values indicate greater clonotype expansion). Boxplots represent the 25th percentile, median, 75th percentile, and 1.5x IQR (whiskers).

nature portfolio

Corresponding author(s):   Andy Minn

Last updated by author(s):   11/03/2022

Reporting Summary

Nature Portfolio wishes to improve the reproducibility of the work that we publish. This form provides structure for consistency and transparency in reporting. For further information on Nature Portfolio policies, see our Editorial Policies and the Editorial Policy Checklist.

Statistics

For all statistical analyses, confirm that the following items are present in the figure legend, table legend, main text, or Methods section.

n/a	Confirmed	
☐	☒	The exact sample size (*n*) for each experimental group/condition, given as a discrete number and unit of measurement
☐	☒	A statement on whether measurements were taken from distinct samples or whether the same sample was measured repeatedly
☐	☒	The statistical test(s) used AND whether they are one- or two-sided *Only common tests should be described solely by name; describe more complex techniques in the Methods section.*
☐	☒	A description of all covariates tested
☐	☒	A description of any assumptions or corrections, such as tests of normality and adjustment for multiple comparisons
☐	☒	A full description of the statistical parameters including central tendency (e.g. means) or other basic estimates (e.g. regression coefficient) AND variation (e.g. standard deviation) or associated estimates of uncertainty (e.g. confidence intervals)
☐	☒	For null hypothesis testing, the test statistic (e.g. *F*, *t*, *r*) with confidence intervals, effect sizes, degrees of freedom and *P* value noted *Give P values as exact values whenever suitable.*
☒	☐	For Bayesian analysis, information on the choice of priors and Markov chain Monte Carlo settings
☐	☒	For hierarchical and complex designs, identification of the appropriate level for tests and full reporting of outcomes
☐	☒	Estimates of effect sizes (e.g. Cohen's *d*, Pearson's *r*), indicating how they were calculated

Our web collection on statistics for biologists contains articles on many of the points above.

Software and code

Policy information about availability of computer code

Data collection	Single cell RNA-seq reads were aligned to the mm10 reference genome and quantified using cellranger count (10X Genomics, version 2.1.0). TCR reads were aligned to the GRCh38 reference genome and consensus TCR annotation was performed using cellranger vdj (10X Genomics, version 2.1.0). Bulk RNA-seq data were aligned to the GRCm38 genome with STAR v2.5.2a. Gene-based quantification was performed with salmon v0.13.1. For ATAC-seq, adapters were trimmed using cutadapt, and reads were aligned to the mm10 genome using Bowtie2. After alignment, duplicate reads and reads mapping to chrM were removed. To correct for the Tn5 offset, bam file reads were shifted ("+" stranded +4 bp, "–" stranded -5 bp). Peak calling was performed with MACS2, and high-confidence peaks were filtered using the irreproducible discovery rate (IDR).
Data analysis	For CD8 T cell activity prediction, the method described by Rooney et al., Cell 2015 was used. Motif enrichment analysis was carried out using HOMER suite. Differential TF activity was examined using chromVAR (v1.6.0). Transcription factor footprints were identified using the footprinting tool from HINT-ATAC. TF motifs were scanned for within footprint regions using FIMO. For bulk RNA-seq data, differential gene expression analysis was carried out using DESeq2 (v1.24.0). GSEA was performed using fgsea (1.10.1). Single cell RNA-seq data was imputed using SAVER (v1.1.2) and analyzed using Seurat (v3.1.2). GSVA (v.1.32.0) was used to identify enriched gene signatures DC subsets or CD8 T cell states. The DC and CD8 T cell interaction analysis was carried out using CellChat (v.1.1.3). Pseudotime analysis was carried out using Monocle 2. TCR alignment was carried out using msa (v1.15.0). Cluster analysis was performed using HDMD (v1.2) and Rphenograph (v.0.99.1).

For manuscripts utilizing custom algorithms or software that are central to the research but not yet described in published literature, software must be made available to editors and reviewers. We strongly encourage code deposition in a community repository (e.g. GitHub). See the Nature Portfolio guidelines for submitting code & software for further information.

Data

Policy information about availability of data

  All manuscripts must include a data availability statement. This statement should provide the following information, where applicable:

    - Accession codes, unique identifiers, or web links for publicly available datasets
    - A description of any restrictions on data availability
    - For clinical datasets or third party data, please ensure that the statement adheres to our policy

> Raw data for Figures 1-7 and Extended Data Figures 1-5 and 7-8 have been deposited in the Sequence Read Archive (SRA) and are available under accession number PRJNA626462. Sequencing data related to Figure 5F have been previously deposited in the GEO under accession number GSE83850.

Human research participants

Policy information about studies involving human research participants and Sex and Gender in Research.

Reporting on sex and gender	n/a
Population characteristics	n/a
Recruitment	n/a
Ethics oversight	n/a

Note that full information on the approval of the study protocol must also be provided in the manuscript.

Field-specific reporting

Please select the one below that is the best fit for your research. If you are not sure, read the appropriate sections before making your selection.

☒ Life sciences   ☐ Behavioural & social sciences   ☐ Ecological, evolutionary & environmental sciences

For a reference copy of the document with all sections, see nature.com/documents/nr-reporting-summary-flat.pdf

Life sciences study design

All studies must disclose on these points even when the disclosure is negative.

Sample size	Prior power calculations using an alpha level of 0.05 and expected effect sizes were used to guide the sample sizes used for mouse studies.
Data exclusions	No data were excluded from analysis.
Replication	All experimental results and conclusions were derived from using independent biological replicates.
Randomization	Mice procured from the same source/vendor were randomly assigned to a treatment group. Sex was not considered.
Blinding	Data collection and analysis were not typically performed blind to the conditions of the experiments.

Reporting for specific materials, systems and methods

We require information from authors about some types of materials, experimental systems and methods used in many studies. Here, indicate whether each material, system or method listed is relevant to your study. If you are not sure if a list item applies to your research, read the appropriate section before selecting a response.

Materials & experimental systems

n/a	Involved in the study
☐	☒ Antibodies
☐	☒ Eukaryotic cell lines
☒	☐ Palaeontology and archaeology
☐	☒ Animals and other organisms
☒	☐ Clinical data
☒	☐ Dual use research of concern

Methods

n/a	Involved in the study
☒	☐ ChIP-seq
☐	☒ Flow cytometry
☒	☐ MRI-based neuroimaging

Antibodies

Antibodies used

All antibodies used are anti-mouse and include: OAS1 (clone E-2, cat. no. sc-365072, Santa Cruz Biotechnology), CD45 conjugated to AF700 (clone 104, cat. no. 109822, BioLegend), TCRβ conjugated to PE/Dazzle 594 (clone H57-597, cat. no. 109239, BioLegend), H-2Kb/H-2Db conjugated to AF647 (clone 28-8-6, cat. no. 114612, BioLegend), I-A/I-E conjugated to Pacific Blue (clone M5/114.15.2, cat. no. 107620, BioLegend), F4/80 conjugated to PE/Cy7 (clone BM8, cat. no. 123113, BioLegend), CD11c conjugated to FITC (clone N418, cat. no. 117306, BioLegend), CD86 conjugated to BV785 (clone GL-1, cat. no. 105043, BioLegend), TIM3 conjugated to BV421 (clone RMT3-23, cat. no. 119723, BioLegend), CX3CR1 conjugated to APC (clone SA011F11, cat. no. 149007, BioLegend), IFNγ conjugated to PE/Dazzle (clone XMG1.2, cat. no. 505845, BioLegend), CD8 conjugated to eFluor450 (clone 53-6.7, cat. no. 48-0081-80, eBioscience), NK1.1 conjugated to APC (clone PK136, cat. no. 17-5941-82, eBioscience), Perforin conjugated to FITC (clone eBioOMAK-D, cat. no. 11-9392-82, eBioscience), PD1 conjugated to PE/Cy7 (clone J43, cat. no. 25-9985-82, eBioscience), CD8 conjugated to FITC (clone KT15, cat. no. D271-4, MBL International Corporation), PD-L1 conjugated to PE (clone MIH5, cat. no. 558091, BD Biosciences), CD11b conjugated to PE (clone M1/7, cat. no. 553311, BD Biosciences). For flow cytometry staining, antibodies were used at 1:50 dilution. For Western blots, a 1:1000 dilution was used. All in vivo antibody treatments (therapy and depletion) were performed at 10 mg/kg.

Validation

All antibodies were validated by the manufacturer, and antibody-specific staining was compared to isotype or no staining control samples.

Eukaryotic cell lines

Policy information about cell lines and Sex and Gender in Research

Cell line source(s)

Melanoma cell line Res 499 and breast cancer cell line Res 237 were derived previously from B16-F10 and TSA respectively. Knockouts were generated using CRISPR-Cas9 technology. CT26 and B16 cell lines were purchased form ATCC. TSA was a kind gift from Dr. Sandra Demaria.

Authentication

Knockouts were confirmed using either Western or flow cytometry.

Mycoplasma contamination

All cell lines were confirmed to be mycoplasma negative.

Commonly misidentified lines
(See ICLAC register)

No commonly misidentified cell lines were used.

Animals and other research organisms

Policy information about studies involving animals; ARRIVE guidelines recommended for reporting animal research, and Sex and Gender in Research

Laboratory animals

Five- to seven-week-old female C57BL/6 (stock# 027) and BALB/c (stock# 28) were obtained from Charles River Laboratory. Five- to seven-week-old female C57BL/6 (stock# 000664), Perforin knockout (C57BL/6-Prf1tm1Sdz/J; stock# 002407), Batf3 knockout (B6.129S(C)-Batf3tm1Kmm/J; stock# 013755) were ordered from Jackson Laboratory (Bar Harbor, ME).

Wild animals

n/a

Reporting on sex

Sex was not considered in the study design and results are not sex-specific.

Field-collected samples

n/a

Ethics oversight

All animal experiments were performed according to protocols approved by the Institutional Animal Care and Use Committee of the University of Pennsylvania.

Note that full information on the approval of the study protocol must also be provided in the manuscript.

Flow Cytometry

Plots

Confirm that:

☒ The axis labels state the marker and fluorochrome used (e.g. CD4-FITC).

☒ The axis scales are clearly visible. Include numbers along axes only for bottom left plot of group (a 'group' is an analysis of identical markers).

☒ All plots are contour plots with outliers or pseudocolor plots.

☒ A numerical value for number of cells or percentage (with statistics) is provided.

Methodology

Sample preparation	Two weeks following tumor injection, tumors were harvested, digested with collagenase IV (EMSCO/Fisher) for 30 minutes at 37 C. The suspension was filtered, treated with ACK lysis buffer (Quality Bio) for 5 minutes on ice. Staining was carried out first in Live/dead fixable aqua dead cell staining kit (Thermo Fisher Scientific) and TruStain fcX (Biolegend) for 15 minutes at 4 °C, followed by surface antibody staining for 30 minutes at 4 °C. Intracellular staining was carried out using Foxp3/Fix/Perm kit (Thermo Fisher Scientific). Antibody working dilutions were 1:50 or empirically determined when needed.
Instrument	Cell sorting was carried out on LSR II or Aria flow cytometer when necessary.
Software	Flow cytometry data were analyzed using Flowjo or with R and Bioconductor.
Cell population abundance	Post-sort purities were assessed by flow cytometry and confirmed to be > 95%. Where applicable, post-sort purities were also validated by single cell RNA-sequencing data.
Gating strategy	Cells were first gated on FSC/SSC, then gated to exclude doublets based on FSC-A/FSC-W. Dead cells were excluded based on LIVE/DEAD Fixable Aqua staining. Cells were categorized as tumor cells (CD45-), CD8 T cells (CD45+TCRb+CD8+), and CD11c DCs (CD45+F4/80-MHCII+CD11c+CD11b-).

☒ Tick this box to confirm that a figure exemplifying the gating strategy is provided in the Supplementary Information.